8-2016

# Localization and delocalization in two-dimensional quantum percolation

Brianna S. Dillon Thomas
*Purdue University*

*Graduate School Form*
*30 Updated 12/26/2015*

**PURDUE UNIVERSITY**
**GRADUATE SCHOOL**
**Thesis/Dissertation Acceptance**

This is to certify that the thesis/dissertation prepared

By Brianna Symons Dillon Thomas

Entitled

LOCALIZATION AND DELOCALIZATION IN TWO-DIMENSIONAL QUANTUM PERCOLATION

For the degree of Doctor of Philosophy

Is approved by the final examining committee:

Hisao Nakanishi
Chair

Erica Carlson

Andrew S. Hirsch

Sabre Kais

To the best of my knowledge and as understood by the student in the Thesis/Dissertation Agreement, Publication Delay, and Certification Disclaimer (Graduate School Form 32), this thesis/dissertation adheres to the provisions of Purdue University's "Policy of Integrity in Research" and the use of copyright material.

Approved by Major Professor(s): Hisao Nakanishi

Approved by: John P. Finley 7/15/2016

Head of the Departmental Graduate Program Date

# LOCALIZATION AND DELOCALIZATION IN TWO-DIMENSIONAL QUANTUM PERCOLATION

A Dissertation

Submitted to the Faculty

of

Purdue University

by

Brianna S. Dillon Thomas

In Partial Fulfillment of the

Requirements for the Degree

of

Doctor of Philosophy

August 2016

Purdue University

West Lafayette, Indiana

"The scientist does not study nature because it is useful to do so. He studies it because he delights in it, and he delights in it because it is beautiful."

Henri Poincaré

*To the many people who instilled in me a love of nature.*

# ACKNOWLEDGMENTS

First and foremost, I must thank my advisor, Professor Hisao Nakanishi, whose gracious guidance has contributed greatly to making the past six years a rewarding experience. He held high standards without being overbearing and was always respectful of my time outside of the physics department, a combination which allowed me to thrive in my research. During our meetings, he knew when to instruct, when to leave me to my own devices, and when to nudge me in a different direction. I have learned a great deal about being a physicist from him, and am grateful to have had him as my advisor. Additionally, my research would not have been possible without the computing resources provided by the Department of Physics and Astronomy on their portion of the Purdue Research Computing (RCAC) clusters. I am also thankful for others in the department, especially Professor Erica Carlson, who readily opened her office for random lengthy conversations and advice about being a woman in physics academia, and Dr. Rebecca Lindell, who encouraged me to further my side interests in education research through seminars, reading groups, and journal clubs.

Looking further back, I am indebted to my undergraduate professors and advisors; I doubt I would have pursued graduate school without the rigorous, student-focused instruction and individual attention of my professors at Grove City College. I am particularly thankful for the countless hours Professors DJ Wagner, Mark Fair, and Shane Brower spent listening to me and helping me figure out my plans for the future. Additionally, I am grateful for my second REU advisor, Professor Richard Scalettar, who introduced me to computational condensed matter theory, and whose enthusiasm, encouragement, and attention over the eight weeks I worked with him re-lit an interest in research that my first REU had nearly quashed.

Lastly, I would not have finished graduate school nearly as happy and healthy as I am were it not for my incredible support network of family and friends within the

physics department, my church, and Graduate IVCF. During the marathon that is graduate school, these people gave my life meaning outside of physics, listened to me, made me smile and relax when I needed it, encouraged me, and prayed for me. Out of the many people who were a part of my life during my time at Purdue, a few stand out: my parents, Daniel and Peggy, for their constant prayers, love, and support; my sister, Erin, for sharing with me the joys and frustrations unique to graduate school; my roommate, Sarah, for sharing the day-to-day of graduate life for two years; my friend Anna, for hours of conversation and walks; and my mentor Emily, for helping me to keep my eyes on the ultimate goal, nurturing my leadership skills, and being an open heart and ear whenever I needed to talk. And last but not least, my husband, Alan, who has been a constant presence from the beginning, first as a friend, and now as my husband. I am ever thankful for his putting up with my unpredictable work schedule, and for his encouragement and steady support over these past six years.

TABLE OF CONTENTS

# LIST OF TABLES

# LIST OF FIGURES

Figure Page

# ABSTRACT

Thomas, Brianna S. Dillon PhD, Purdue University, August 2016. Localization and Delocalization in Two-Dimensional Quantum Percolation. Major Professor: Hisao Nakanishi.

Quantum percolation is one of several disorder-only models that address the question of whether conduction, or more generally, delocalization, is possible in two dimensional disordered systems. Whether quantum percolation exhibits a delocalization-localization phase transition in two dimensions is an ongoing debate, but many recent studies point toward there being a delocalized phase at non-zero disorder, in contradiction to the behavior of the Anderson model, another disorder-only model. In this dissertation, I present my research on quantum percolation that shows a delocalized state is possible, both on isotropic lattices and on highly anisotropic lattices, and shows that the essential characteristics of the quantum percolation model are maintained even when the model is modified to allow tunneling through diluted sites. In Chapter 1, I provide an overview of the scaling theory for the Anderson model, the history of the quantum percolation model, and the computational methods used to study the quantum percolation model in two dimensions. In Chapter 2, I study the two-dimensional quantum percolation model with site percolation on isotropic square lattices using numerical calculations of the transmission coefficient $T$ on a much larger scale and over a much wider range of parameters than was done previously. I confirm the existence of delocalized, power-law localized, and exponentially localized phases, and determine a detailed, quantitative phase diagram for energies $0.001 \leq E \leq 1.6$ and dilutions $2\% \leq q \leq 38\%$. Additionally, I show that the delocalized phase is not merely a finite size effect. In Chapter 3, I examine the same 2D quantum percolation model on highly anisotropic strips of varying width, to investigate why the isotropic lattice results show a delocalized phase, unlike work by others on anisotropic strips,

in particular that of Soukoulis and Grest [Phys. Rev. B **44**, 4685 (1991)] using the transfer matrix method . The model is studied over a dilution range extending to lower dilutions than those studied by Soukoulis and Grest, and I find evidence of a delocalized phase at these low dilutions, with phase boundaries that agree with my previous work. In Chapter 4, I modify the 2D quantum percolation model to allow for tunneling through and between diluted sites by making the hopping integral for diluted sites be a non-zero fraction of the hopping integral for occupied sites, while yet maintaining a binary disorder. Using numerical calculations of the transmission coefficient $T$ as in Chapter 1, I determine a complete, detailed three-parameter phase diagram showing the effects of energy $E$, dilution $q$, and hopping integral $w$. I find that the three phases characteristic of quantum percolation persist for a fairly large range of $w$ before the entire system becomes delocalized at sufficiently large $w$. Additionally, I examine the inverse participation ratio (IPR) to gain a complementary picture of how the particle's wave function changes with respect to $q$ and $w$. Lastly, in Chapter 5 I present my analysis and conclusions.

# 1. INTRODUCTION AND COMPUTATIONAL METHODS

The study of the metal-insulator transition, or more broadly, the delocalization-localization transition, can be roughly divided into the study of two effects: localization due to electron-electron interactions, and localization due to the disorder of the underlying material. Localization due to disorder only is often called Anderson localization, named after the Anderson model, which is one of the earliest theoretical models for disordered systems in the absence of interactions. The quantum percolation model is another model that accounts for only the effects of disorder, and is of particular interest because the behavior it models in two dimensions contradicts the expectations set forth by studies of the Anderson model. In 1979, E. Abrahams et al. used scaling theory to predict that even a very small amount of disorder in a two-dimensional system would prevent conduction [1], a prediction which proved true for the original Anderson model, and was initially expected to be valid for other disorder-only models. However, various studies, including my research presented here, have shown that adding disorder in the quantum percolation model does not always result in localization. Before exploring the quantum percolation model in detail, we must first step back and review the Anderson model findings, the classical percolation model, and the history of quantum percolation model studies.

## 1.1 The Anderson model and one-parameter scaling

The Anderson model, proposed in 1958 by P.W. Anderson [2], is a simplified model of quantum transport in a disordered medium. It ignores such factors as the spin of the particle, particle-particle interactions, and external fields, and considers only the

effects of randomness introduced in the energy of lattice sites. The hamiltonian has the form:

$$H = \sum_i \epsilon_i |i\rangle\langle i| + \sum_{<ij>} V_{ij}(|i\rangle\langle j| + |j\rangle\langle i|) \tag{1.1}$$

where $\epsilon_i$ is the on-site energy of the particle, assigned randomly according to some probability distribution of width $W$ (the most common being a box distribution $\frac{1}{W}$, and $V_{ij}$ is a fixed site hopping energy between nearest neighbor sites only. Although the Anderson model is most frequently studied with disordered on-site energy and fixed hopping energy, it has also been studied with fixed on-site energy and random hopping energy, as for example in Ref. [3]. In either case, the distinguishing characteristic of the Anderson model is that the disorder of the system has a finite mean and variance, and the strength of the disorder is characterized by the ratio $\frac{V}{W}$.

In 1979, E. Abrahams et al. published a landmark paper on the one-parameter scaling theory of localization for the Anderson model in d dimensions. [1] In it, they studied the behavior of the generalized, dimensionless conductance of a disordered electronic system, defined as

$$g(L) = \frac{\delta E(L)}{dE(L)/dN} = \frac{G(L)}{e^2/2\hbar} \tag{1.2}$$

where $G(L)$ is the conductance of a hypercube of dimension $d$ with macroscopic side $L$, $dE(L)/dN$ is its mean energy level spacing, and $\delta E$ is the mean of the energy fluctuations induced by changing the boundary conditions of the hypercube lattice. When two hypercubes are fitted together, the ratio $g(L)$ determines the change in the energy levels. Abrahams et al. then combined $b^d$ cubes to make a new, larger cube of side $bL$, and proposed that the conductance for the large cube is

$$g(bL) = f(b, g(L)). \tag{1.3}$$

This was rewritten as

$$\frac{d \ln g(L)}{d \ln L} = \beta(g(L)) \tag{1.4}$$

where *beta* is the scaling function.

Finally, physical arguments were used to determine the asymptotic values for $\beta(g(L))$ and perturbation theory to estimate the rest of the function, the results of which are shown in Fig. 1.1.

As seen in the figure, for dimensions $d > 2$, $\beta$ crosses $\ln g$ at a critical value of conductance $g_c$, which indicates a transition from a conducting (delocalized) state (for $\beta > 0$) to an insulating (localized) state (for $\beta < 0$). In $d < 2$ dimensions, unsurprisingly, $\beta < 0$ always, indicating the state is always localized for any amount of disorder. In two dimensions, $\beta < 0$ as well. Although there is logarithmic behavior for small $L$, it is not a true metallic state and crosses over to exponential localization as $L \to \infty$. From this, Abrahams et al. concluded that disorder prevents conduction for dimensions $d \leq 2$. Various studies confirmed this result in the years soon after this paper (see, for a few examples, Ref. [4–6]), and the Anderson model has continued to

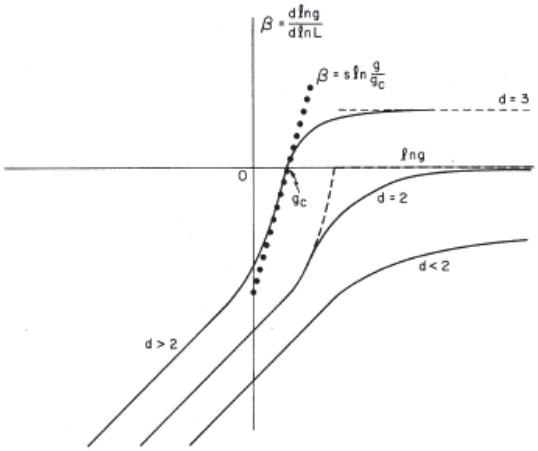


Figure 1.1. Reproduced from Ref. [1]. Plot of $\ln \beta$ vs. $\ln g$ in $d < 2$, $d = 2$, and $d > 2$ dimensions.

be a rich field of study. More recent work has shown additional variations, including work relatively recent work by Goldenfeld and Haydock [7], who found a transition between different non-conducting states at non-zero disorder in two dimensions, even though there was no transition to conducting behavior with disorder; and by Eilmes et al [3] on the Anderson model with of-diagonal disorder, who found that the localization length in 2D diverges at $E = 0$, indicating some amount of non-localized states.

## 1.2 The classical percolation model

Quantum percolation is derived from the classical percolation model, a statistical model for the transmission of a classical particle on a disordered lattice. The percolation model gets its name from the way disorder is modeled. "Percolation" simply means the movement of one substance through another substance that has many small holes in it at random locations (a familiar real-world example being water percolating through coffee grounds to brew coffee). In the percolation model, disorder is created by diluting the lattice in one of two ways: by removing sites (site percolation), or by removing bonds between sites (bond percolation), as depicted in Fig. 1.2a and b respectively. In doing so, we create many small "holes" on the lattice that impede the transmission of a particle traveling through the lattice. In both site and bond percolation, the only way a particular disordered lattice can transmit a particle is if there is a fully connected path from one end of the lattice to the other (for instance from the upper left corner to the lower right corner in Fig. 1.2a). Thus, a perfectly ordered lattice will have complete transmission, since all sites and bonds are connected, while a lattice with a sufficiently high dilution will have no transmission, since all possible paths from one side of the lattice to the other will lead to dead ends.

Thus far we have described classical percolation on individual finite-sized lattice examples, but to properly study it we must consider the average behavior of all different disorder realizations for a variety of disorders in the thermodynamic limit.

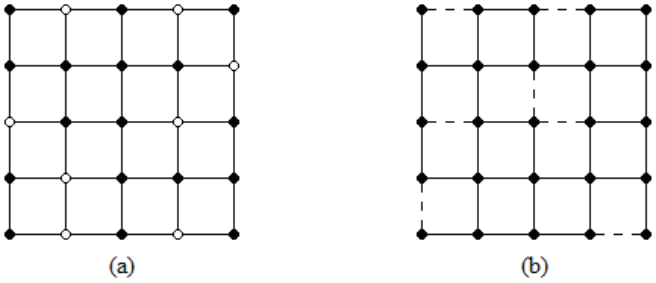


Figure 1.2. Examples of (a) site disordered and (b) bond disordered lattices. Removed sites (bonds) are given by open circles (dotted lines).

There are two factors to consider as we increase dilution from zero: 1) the probability that arbitrarily chosen input and output points on a lattice are connected, and 2) the overall phase of the model. With the former, as we introduce disorder, the probability that the arbitrarily chosen input and output points are connected at a given dilution $q = 1 - p$ decreases, since the particle cannot travel through a diluted/ "unavailable" site or bond. Thus, the average transmission measured on lattices at that dilution $q$ will also decrease. However, the lattice at dilution $q$ is still considered conducting if there exists *any* infinite connected path across the lattice, although it may not necessarily be between the arbitrarily prescribed input and output points. As dilution is increased, the probability of the chosen input and output points being connected decreases smoothly while the probability of finding an infinite connected path remains 100%, until a critical dilution percentage of $q_c = 1 - p_c$. At the critical dilution, enough sites (or bonds) have been removed that not only is there zero probability that the chosen input and output are connected, but also the probability of finding *any* connected path drops discontinuously to 0; regardless of the input and output points chosen, there is no connected path across the lattice anywhere. Thus at and above this critical dilution, the classical percolation model is said to be no

longer conducting. For classical percolation on a square lattice, this occurs at about $p_c \simeq 0.59$ for site percolation and $p_c = 0.50$ for bond percolation.

### 1.3 The quantum percolation model

The quantum percolation model modifies the classical model in one significant way: the particle whose transport is being studied is a quantum-mechanical quasi-particle. The wave-like nature of a quantum particle introduces interference effects which can influence the particle's transport, even if the underlying lattice is diluted in the same way as in the classical model. The Hamiltonian for the quantum percolation model is constructed so as to create the site and bond percolation disorder setup used for the classical percolation model. It can be written in the same form as the Anderson model's Hamiltonian (Eq. 1.1), but the disorder is applied differently. For site percolation, the hopping integrals $V_{ij}$ are held constant and randomness is introduced through the on-site energy $\epsilon_i$, which takes on values of 0 for available sites and $\infty$ for unavailable/diluted sites (the solid dots and open dots in Fig. 1.2a, respectively) – the infinite energy barrier on the diluted sites makes it impossible for the particle to travel through those sites, just as it is unable to travel through a removed site in the classical case. For bond percolation, the on-site energy $\epsilon_i$ is held constant and randomness is introduced through the hopping integrals $V_{ij}$, which have values of 1 or 0 depending on whether the bond between sites $i$ and $j$ is present or has been removed, respectively. Again, the 0 hopping integral for absent bonds makes it impossible for a particle on site $i$ or $j$ to be able to jump to the other site, just as a particle cannot move between two sites in the classical case if there is no bond between them. Note that for both site percolation (diagonal disorder) and bond percolation (off-diagonal disorder), the disorder in the quantum percolation model is represented by a binary distribution which creates impenetrable barriers around certain sites, in contrast to the Anderson model's distribution with finite mean and variance.

As mentioned, the transmission of a quantum particle through a site (bond) percolated lattice is more complex than that of a classical particle, due to the way a quantum particle interacts with the diluted sites (bonds) and interferes with itself. Whereas classically, the existence of an infinite connected path across a diluted lattice was the only criterion for conduction, here there is some probability that the particle may not be transmitted, since its wave function will reflect off the infinite-energy barriers created by the diluted sites (bonds) and interfere with itself. Thus there is some probability that the particle will be transmitted through the lattice as a whole and some probability that it will be reflected; we can also think of this as saying the particle will be only partially transmitted. In fact, due to the boundary conditions imposed in these studies, even a perfectly ordered (i.e. fully connected) lattice may not have perfect transmission, depending on the energy of the particle. [8] Thus to determine phase of the quantum percolation model, one must consider the physical extent of the particle wave function - whether it is extended throughout the lattice or localized (strongly or weakly) around a few sites. There are many techniques one can use to do this; our methods will be discussed in Section 1.6. Because of the interference effects present in the quantum percolation model, we expect the delocalization-localization transition to occur at a lower critical dilution percentage $q_q \leq q_c$, if it exists at all.

Due to its similarities with the Anderson model, it was initially thought that the quantum percolation model would follow the same scaling law described in Section 1.1 for the Anderson model; that is, that a localization-delocalization transition was possible for $d > 2$ but not for dimensions $d \leq 2$. Indeed, for three dimensions this seemed to be the case. Work in three dimensions includes that by Soukoulis et al. using transfer matrix calculations on a simple cubic lattice over the entire possible energy range [9], Koslowski and von Neissen using the Thouless-Edwards-Licciardello method [10], and Chang et al. using series expansion calculations [11], all of whom found a critical percentage $p_q$ above which states became delocalized. However, when Chang et al. computed the localization length critical exponent $\nu$ for

the localized region, used to help determine the universality class of a system, they found it to be significantly different from the value of $\nu$ for the Anderson model in three dimensions, to a degree that was unlikely to be accounted for by possible numerical error. These results strongly suggested that the quantum percolation model is in a different universality class than the Anderson model, a possibility that is reflected in the lack of agreement over whether quantum percolation exhibits a localization-delocalization transition in two dimensions or not.

Among those who found delocalization to be impossible with disorder in two dimensions there are two groups: those who only observed (or only made mention of) one type of localized behavior, and those who observed a transition from strong to weak localization at some dilution $q_q = 1 - p_q$. Soukoulis and Grest, mentioned above, fall into the first group. They followed up their work in three dimensions with numerical finite-size scaling on two dimensional strips of varying widths to measure the localization length $\lambda$, which they found to diverge as $p \to 1$ according to the form $\lambda = A \exp^{B[p/(1-p)]^{1/2}}$, implying that all states are exponentially localized for any amount of disorder. [12] Using other numerical methods, Mookerjee et al. and Hałdaś et al. likewise concluded that there are no delocalized states except for zero disorder, though they made no mention of the strength of the localization. [13, 14] Within the second group, studies using such techniques as real space renormalization [15], computation of the inverse participation ratio [16], the Thouless-Edwards-Licciardello method [10], and series expansions [17] showed that while the particle state was delocalized only for fully ordered systems, there was a transition from exponential (strong) localization to a weaker localization for $p_q$ within the range $0.70 \leq p_q \leq 0.87$ depending on the type of disorder (site or bond) and energy of the particle.

On the other hand, several more recent studies by various groups seem to indicate that, in addition to a possible transition between localized states, there is in fact a transition to a delocalized state for non-zero disorder. The techniques used to arrive at this conclusion are varied, including wave propagation through the lattice [18], Chebychev expansions examining the time evolution of particle states [19], numerical

calculations of transmission [8, 20, 21], and von Neumann entropy calculations [22]. Among those who specified the critical dilution, the transition to a delocalized state was observed within a wide range depending on the energy, $0.67 \leq p_q \leq 0.95$, with a secondary transition between strongly and weakly localized states for some lower percentage sometimes observed.

Clearly, there is not yet consensus on the localization behavior of the quantum percolation model in two dimensions. Although much recent work leans toward there being a delocalized state for at least some energies, reports of exactly where that transition occurs vary widely, and there are still some who still hold that extended states are not possible except in a perfectly ordered system (e.g. Ref [14]). Furthermore, among those who examined the localization length critical exponent, estimates vary across an order of magnitude within the range $0.2 \leq \nu \leq 3.35$, apparently depending on not only the disorder type (site or bond) but also the energy. Since the critical exponents are used to determine the universality class of a system, such wide-ranging estimates do not help settle the matter of whether or not we should expect the quantum percolation model to behave similarly to the Anderson model. In Chapters 2 and 3 we build off of previous work in our group and examine the localization question in detail.

### 1.4 The quantum percolation model with modified hopping integrals

As discussed in the previous section, the Anderson model and the quantum percolation model are distinguished by the distribution from which the on-site and/or off-diagonal disorder is drawn: a finite, continuous distribution for the Anderson model, and a binary distribution of either zero or infinite energy barriers for the quantum percolation model. Since many studies point toward quantum percolation having qualitatively different transport behavior than the Anderson model in two dimensions, we decided to investigate how differences in the nature of the disorder in the two models might lead to these differences, after further investigating the ques-

tion of a phase transition in detail ourselves. To do this, we consider a modified quantum percolation model in which the binary nature of the quantum percolation model's disorder is maintained, while changing the distribution to a finite one that allows tunneling between available and "unavailable" sites. In essence, we change the hopping integral such that instead of completely removing some percentage of bonds to disconnect sites from the rest of the lattice, we instead merely weaken some of them by a uniform amount. If the infinite-energy aspect of quantum percolation disorder is more important, we expect that changing to a finite energy will result in changing the phase behavior of the quantum percolation model, but not if the binary aspect (which is maintained) is the more important characteristic. We explore this modified model in detail in Chapter 4.

## 1.5 Experimental relevance

Experimental studies of two-dimensional disordered systems have also contested the scaling theory of localization proposed by Abrahams et al. For example, Kravchenko et al. [23–25] studied the resistivity of high-mobility Si MOSFETs with varying low electron densities in absence of an external magnetic field. Above a critical electron density $n_c r$, they observed the resistivity to undergo an order of magnitude drop as the temperature $T \to 0$, while below the critical density the resistivity increased monotonically with decreasing temperature. These results suggested that there is a metal-insulator transition in the $T = 0$ limit (the limit in which Abrahams' scaling theory applies) as the carrier density is decreased past the critical density. Furthermore, they were able to scale the resistivity with respect to temperature T both above and below the critical electron density; such scaling behavior is indicative of a phase transition. Although Kravchenko et al. did not discuss their experimental findings in relation to the quantum percolation model specifically, their results did call into question the predictions of scaling theory. For a detailed review of similar experiments, see Ref. [26].

More recent work has shown connections between various experimental systems and quantum percolation. Zhang et al. [27] and Becker et al. [28] studied thin magnatite films using magnetic force microscopy and scanning tunneling spectroscopy, respectively. Such films have a ferromagnetic conducting ground state, but become insulating at higher temperatures. The two groups examined the conducting and insulating domains as temperature was increased and found that doing so caused the insulating domains to grow, behavior which is analogous to disconnected clusters of sites becoming increasingly larger in the percolation model. Another striking example is found in granular metal films, in which the tunnel junction conductance between grains are distributed randomly. Feigel'man, Ioselevich, and Skvortsov [29] demonstrated that the behavior of such a material is essentially percolative, with a metal-insulator transition taking place when the conductance of enough junctions have dropped to zero. Lastly, Cheianov et al [30] used a variant of the percolation model, in which bonds are represented by current-carrying resistors, to model the conductivity of undoped graphene. They showed that charge-neutral graphene can be viewed as containing "puddles" of electrons and holes, with the conductivity determined by random links between them rather than the conductivity of individual "puddles".

## 1.6 Computational methods

### 1.6.1 Schrödinger equation and the Daboul ansatz

The quantum percolation model with zero onsite energy is described by the Hamiltonian

$$H = \sum_{<ij>} V_{ij} |i\rangle\langle j| + c.c. \tag{1.5}$$

where $|i>$ and $|j>$ are tight-binding functions for the lattice sites $i$ and $j$, $V_{ij}$ is the hopping matrix element between the lattice sites, and the sum is over nearest

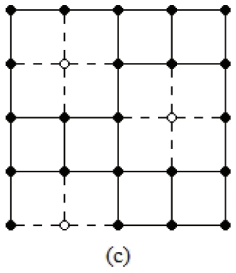


Figure 1.3. Example of the hybrid site dilution model used in this research. Removed sites (bonds) are given by open circles (dotted lines).

neighbor pairs. In this work, I study a variation on the site-dilution case in which sites are removed with probability $q$, which at the same time removes their nearest-neighbor bonds, as illustrated in Fig. 1.3. Mathematically, if both sites i and j are available, $V_{ij}$ is equal to some constant $V_0$, otherwise it is zero. Since the energy of the system scales as $V_0$, it is generally convenient to set $V_0 = 1$. For the modified quantum percolation model discussed in Section 1.4, we change this slightly by setting $V_{ij} = w$ for $i$ and/or $j$ unoccupied, where $0 \leq w \leq 1$ and $w$ is the same for all diluted sites, which enables the desired tunneling through and among diluted sites while still maintaining a binary disorder.

To calculate the transmission of a quantum particle through this lattice, we attach semi-infinite one-dimensional input and output leads to opposite sides of the lattice; the simplest such connection is a point-to-point connection at diagonally opposite corners, as shown in Fig. 1.4 for a toy example of the original model on a fully-connected lattice.

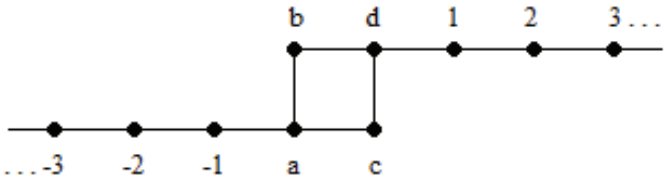


Figure 1.4. A 2x2 ordered lattice with semi-infinite leads attached to diagonally opposite corners.

The wavevector for the entire system used in the time-independent Schrodinger equation $H\psi = E\psi$ can then be written as

$$\begin{pmatrix}
\ddots & \vdots & \vdots & \vdots & \vdots & \vdots & \vdots & \vdots & \vdots & \vdots & \vdots & \\
\dots & -E & 1 & 0 & 0 & 0 & 0 & 0 & 0 & 0 & 0 & \dots \\
\dots & 1 & -E & 1 & 0 & 0 & 0 & 0 & 0 & 0 & 0 & \dots \\
\dots & 0 & 1 & -E & 1 & 0 & 0 & 0 & 0 & 0 & 0 & \dots \\
\dots & 0 & 0 & 1 & -E & 1 & 1 & 0 & 0 & 0 & 0 & \dots \\
\dots & 0 & 0 & 0 & 1 & -E & 0 & 1 & 0 & 0 & 0 & \dots \\
\dots & 0 & 0 & 0 & 1 & 0 & -E & 1 & 0 & 0 & 0 & \dots \\
\dots & 0 & 0 & 0 & 0 & 1 & 1 & -E & 1 & 0 & 0 & \dots \\
\dots & 0 & 0 & 0 & 0 & 0 & 0 & 1 & -E & 1 & 0 & \dots \\
\dots & 0 & 0 & 0 & 0 & 0 & 0 & 0 & 1 & -E & 1 & \dots \\
\dots & 0 & 0 & 0 & 0 & 0 & 0 & 0 & 0 & 1 & -E & \dots \\
 & \vdots & \vdots & \vdots & \vdots & \vdots & \vdots & \vdots & \vdots & \vdots & \vdots & \ddots
\end{pmatrix}
\begin{pmatrix}
\vdots \\ \psi_{-3} \\ \psi_{-2} \\ \psi_{-1} \\ \psi_a \\ \psi_b \\ \psi_c \\ \psi_d \\ \psi_1 \\ \psi_2 \\ \psi_3 \\ \vdots
\end{pmatrix}
=
\begin{pmatrix}
\vdots \\ 0 \\ 0 \\ 0 \\ 0 \\ 0 \\ 0 \\ 0 \\ 0 \\ 0 \\ 0 \\ \vdots
\end{pmatrix} \tag{1.6}$$

Having infinite leads is obviously intractable numerically, but using an ansatz proposed by Daboul et. al. we can reduce the system to a finite one which includes only the cluster and the lead sites closest to it. [17] According to this ansatz the incoming particle is taken to be a plane wave, part of which is reflected back and part of which is transmitted through the output lead:

$$\begin{aligned}\psi_{-(n+1)} &= e^{-in\kappa} + re^{in\kappa} \\ \psi_{n+1} &= te^{in\kappa}\end{aligned} \tag{1.7}$$

for n=0, 1, 2,... Inserting this ansatz into Eq. 1.6 we can solve for the relationship between $\kappa$ and $E$ by adding the 2nd and 8th rows of the matrix product:

$$\begin{aligned}&(\psi_{-3} - E\psi_{-2} + \psi_{-1}) + (\psi_1 - E\psi_2 + \psi_3) = 0 \\ &(\psi_{-3} + \psi_3) + (\psi_{-1} + \psi_1) - E(\psi_{-2} + \psi_2) = 0 \\ &e^{-i2\kappa} + e^{i2\kappa} + 2 - E(e^{-i\kappa} + e^{i\kappa}) = 0 \\ &(e^{-i\kappa} + e^{i\kappa})^2 - E(e^{-i\kappa} + e^{i\kappa}) = 0 \\ &E = e^{-i\kappa} + e^{i\kappa} \iff \kappa = arccos(E/2)\end{aligned} \tag{1.8}$$

This restricts the energy to $-2 \leq E \leq 2$; adding the one-dimensional chains forces the system to obey the 1D energy band limits, which is half the range able to be explored in 2D ($-4 \leq E \leq 4$ in two dimensions). Despite this restriction, we should still be able to learn a great deal about the transport properties of the system.

The recursiveness of the anzatz also allows us to simplify the infinite system of equations given in Eq. 1.6 to a finite set of equations:

$$\begin{pmatrix} 1 & -E & 1 & 0 & 0 & 0 & 0 & 0 \\ 0 & 1 & -E & 1 & 1 & 0 & 0 & 0 \\ 0 & 0 & 1 & -E & 0 & 1 & 0 & 0 \\ 0 & 0 & 1 & 0 & -E & 1 & 0 & 0 \\ 0 & 0 & 0 & 1 & 1 & -E & 1 & 0 \\ 0 & 0 & 0 & 0 & 0 & 1 & -E & 1 \end{pmatrix} \begin{pmatrix} e^{-i\kappa} + re^{i\kappa} \\ 1 + r \\ \psi_a \\ \psi_b \\ \psi_c \\ \psi_d \\ t \\ te^{i\kappa} \end{pmatrix} = \begin{pmatrix} 0 \\ 0 \\ 0 \\ 0 \\ 0 \\ 0 \\ 0 \\ 0 \end{pmatrix} \tag{1.9}$$

which after some rearranging becomes the square matrix corresponding to the cluster (sites a, b, c, d in our example) and the closest lead sites ($n = \pm 1$):

$$\begin{pmatrix} -E+e^{i\kappa} & 1 & 0 & 0 & 0 & 0 \\ 1 & -E & 1 & 1 & 0 & 0 \\ 0 & 1 & -E & 0 & 1 & 0 \\ 0 & 1 & 0 & -E & 1 & 0 \\ 0 & 0 & 1 & 1 & -E & 1 \\ 0 & 0 & 0 & 0 & 1 & -E+e^{i\kappa} \end{pmatrix} \begin{pmatrix} 1+r \\ \psi_a \\ \psi_b \\ \psi_c \\ \psi_d \\ t \end{pmatrix} = \begin{pmatrix} e^{i\kappa}-e^{-i\kappa} \\ 0 \\ 0 \\ 0 \\ 0 \\ 0 \end{pmatrix} \tag{1.10}$$

This is an exact expression for the Schrödinger equation for a 2x2 ordered system with 1D chains attached, which can be solved to find the reflection and transmission $R = |r|^2$ and $T = |t|^2$. It can be generalized to any $M \times N$ square lattice with disorder; the generalized form of the reduced Schrödinger equation can be written as an $(M^2+2) \times (N^2+2)$ matrix equation of the form

$$\begin{bmatrix} -E+e^{i\kappa} & \vec{c_1}^t & 0 \\ \vec{c_1} & \mathbf{A} & \vec{c_2} \\ 0 & \vec{c_2}^t & -E+e^{i\kappa} \end{bmatrix} \begin{bmatrix} 1+r \\ \vec{\psi}_{clust} \\ t \end{bmatrix} = \begin{bmatrix} e^{i\kappa}-e^{-i\kappa} \\ \vec{0} \\ 0 \end{bmatrix} \tag{1.11}$$

where $\mathbf{A}$ is an $M^2 x N^2$ matrix representing the connectivity of the cluster (with $E$ as its diagonal components), $\vec{c_i}$ is the $(M \times N)$ component vector representing the coupling of the leads to the corner sites, and $\vec{\psi}_{clust}$ and $\vec{0}$ are also $M \times N$ component vectors, the former representing the wave function solutions (e.g. on sites *a-d* in Fig. 1.4). The cluster connectivity in $\mathbf{A}$ is represented with $V_{ij} = 1$ in positions $A_{ij}$ and $A_{ji}$ if $i$ and $j$ are connected, otherwise 0 or $w$ for the original and modified quantum percolation models, respectively, as described at the beginning of the section. As with the toy example, Eq. 1.11 is the exact expression for the 2D system with continuous eigenvalues restricted to the range $-2 \leq E \leq 2$ by the last line of Eq. 1.8, from which the transmission ($T$) and reflection ($R$) coefficients are calculated by $T = |t|^2$ and $R = |r|^2$.

In this work, I apply the model in three ways: in Chapter 2, I study the original model on $L \times L$ lattices of various sizes over six energies $0.001 \leq E \leq 1.6$ and

dilutions $2\% \leq q \leq 38\%$; in Chapter 3 I study the original model on highly anisotropic lattices of width $M$ and length $N$ for three energies $0.05 \leq E \leq 1.05$ and dilutions $2\% \leq q \leq 50\%$; and in Chapter 4 I study the modified percolation model on $L \times L$ lattices for six energies $0.001 \leq E \leq 1.6$, dilutions $2\% \leq q \leq 50\%$, and up to 32 diluted-site hopping energies $0 \leq w \leq 1$. The numerical implementations of the model in these context can be found in the Appendices.

### 1.6.2 Determining localization: Transmission coefficients

The first and primary method used in this work to determine the localization of the quantum percolation model with site disorder is examining how transmission scales with system size, following the approach described by Islam and Nakanishi in Ref. [21]. For each energy $E$ and dilution $q$ (and diluted-site hopping integral $w$, for the modified quantum percolation model) we compute the average transmission $T$ of a particular $L \times L$ or $M \times N$ square lattice, averaging over 500-3000 disorder realizations depending on the lattice size and dilution of the model. For each realization we keep the 9 sites nearest the input and output corners present to ensure the quantum particle actually enters the lattice. We repeat these calculations for successively larger lattice sizes, then plot and fit the curve $T$ vs $L$ (or vs $M$ or $N$).

The best fit of the transmission curve indicates the localization behavior of the system at the specified ($E$, $q$) (or $E$, $q$, $w$ triad). Typically, the strength of localization is used in reference to the rate at which the particle wave function decays with distance. However, since transmission is directly connected to the extent of the particle (if the wave function does not extend to the output point, it has not been transmitted all the way through the lattice), transmission will follow the same pattern. Thus the transmission calculations are analogous to fixing the input on an infinite lattice, sending in a particle, and probing the lattice at successively further away output points until we find the distance at which the wave function is no longer

present. The rate at which the transmission decreases, then, also characterizes the localization state.

From Ref. [21] we expect the largest dilutions to be characterized by an exponential fit ($T = a\exp(-L/l)$, where $l$ is the localization length), meaning the state is exponentially localized. For the lowest dilutions, we expect to find an exponential with offset fit being best ($T = a\exp(-bL) + c$), suggesting the state is delocalized, since even at infinite system size there should still be a non-zero residual transmission given by the offset $c$. Lastly, for dilutions somewhere in the middle range, Ref. [21] found the transmission curves to be best fit by a power law ($T = aL^{-b}$), suggesting a weaker localized state. It is important to note that they sometimes had to plot the transmission curves in different scales (linear vs. log-log) in order to determine the best fit type. In addition to the fits proposed by Islam and Nakanishi, we also tried a power law with offset fit ($T = aL^{-b} + c$), which would also suggest a delocalized state and is a reasonable option given Islam and Nakanishi's observed pure power law region, and a modified exponential fit $T = a\exp(-b(\ln L)^{1/2})$) proposed by Ziman [31] for asymptotically low dilution at the band center on a bipartite lattice, which would be indicative of localization that decays slower than power law.

### 1.6.3 Determining localization: Inverse Participation Ratio

From the wave function solutions of Eq. 1.11 we also calculate the Inverse Participation Ratio (IPR), which measures the fractional size of the particle wave function across the lattice and gives a picture of the transport complementary to the picture provided by the transmission coefficient alone. The IPR is defined by:

$$IPR = \frac{1}{\sum_i |\psi_i|^4 (M * N)} \tag{1.12}$$

where $\psi_i$ is the amplitude of the normalized wave function for the main-cluster portion of the lattice on site $i$ and $M \times N$ is the size of the lattice ($M$ and $N$ may be equal). For our model, we have chosen to normalize the IPR by the lattice size

rather than connected cluster size (as is sometimes done) since the lattice size is the fixed parameter and doing so allows better comparison between different sizes when extrapolating to the thermodynamic limit. (It should also be noted that there are some inconsistencies in how the IPR is defined; some papers define Eq. 1.12 as the participation ratio not the inverse participation ratio.) One should also recall that our $\vec{\psi}$ for given $E$ is a continuum eigenstate of the system containing the 1D lead chains, and $\vec{\psi}_{clust}$ is expected to correspond to a mixed state consisting of eigenstates of the middle square portion of the lattice. We see that given two lattices of the same size, the one with the smaller IPR has the particle wave function residing on a smaller number of sites, though the precise geometric distribution cannot be known from the IPR alone. Although the IPR is certainly influenced by the lattice's amount of disorder, two different disorder realizations may result in very different IPR, thus we calculate not just the average IPR but also the IPR distribution across all realizations. The IPR is often used to assess localization by extrapolating it to the thermodynamic limit; if the IPR approaches a constant fraction of the entire lattice, there are extended states, whereas if it decays to zero the states are localized. However, various studies have shown that IPR as a function of other parameters such as energy can also signal a phase change (see Islam and Nakanishi [8], Johri and Bhatt [32, 33], and Wang et al. [34] for examples in several different systems), thus we will examine the IPR not just with respect to lattice size, but also with respect to other parameters such as dilution.

It is sometimes more instructive to examine the histogram of the IPR across all realizations at a given set of parameters than it is to examine the average IPR alone. In some cases, we may examine just a few distributions, but in other cases we want to know the behavior of the distribution as those parameters change, in which case visually checking all histograms for all parameters becomes cumbersome. In these latter cases we characterize each distribution by its skewness and kurtosis, which measure the symmetry and shape of the distribution, respectively. The skewness of a distribution with $n$ elements $x_i$ is defined by

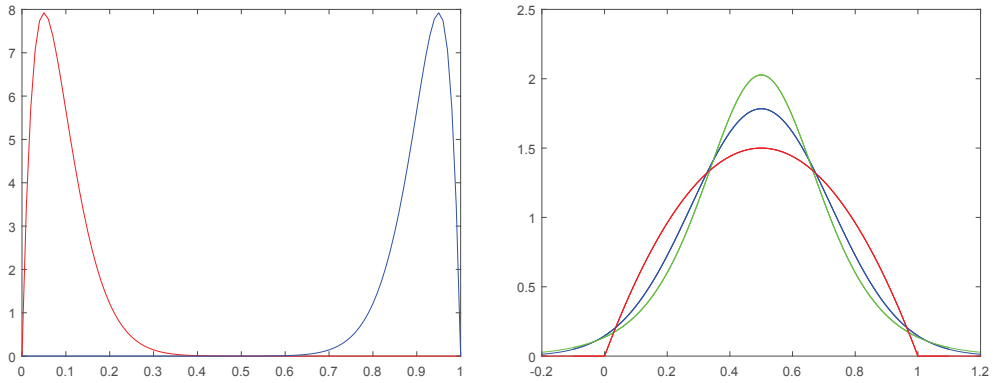


(a) (b)

Figure 1.5. Examples of distributions with different (a) skewness and (b) kurtosis. In (a) the left-hand distribution has positive skewness while the right hand one has negative skewness. In (b), all three distributions have the same mean and variance, but have positive (green), zero (blue), and negative (red) kurtosis.

$$Sk = \frac{\frac{1}{n}\sum_i (x_i - \mu)^3}{\sigma^3} \tag{1.13}$$

where $\mu$ is the mean of $x$ and $\sigma$ is its standard deviation. Skewness $= 0$ for a symmetric distribution, while positive or negative skewness indicates a tail on the right or left side respectively, and $|Sk| > 1$ is generally taken to indicate a substantially asymmetrical distribution. The kurtosis of a distribution is defined by

$$K = \frac{\frac{1}{n}\sum_i (x_i - \mu)^4}{\sigma^4} - 3 \tag{1.14}$$

where $\mu$ and $\sigma$ are again the mean and standard deviation. Kurtosis $= 0$ for a normal distribution, negative kurtosis indicates a flat, more uniform distribution, and positive kurtosis indicate a strongly peaked distribution. A few examples of distributions with different skewness and kurtosis are given in Fig. 1.5.

# 2. LOCALIZATION PHASE DIAGRAM OF TWO-DIMENSIONAL QUANTUM PERCOLATION

The first portion of my research entailed mapping out a detailed phase diagram of the original quantum percolation model with site dilution on square lattices. The work follows the approach of Islam and Nakanishi [21], which sets up the problem using the direct calculation of transmission as described in Chapter 1 Section 1.6.1. However, I studied the problem on a much larger scale and over significantly wider ranges of parameters, which was made possible by performance optimization of the computer code used to calculate the transmission. This allows us to map out large parts of the localization phase diagram of 2D quantum percolation quantitatively, not merely qualitatively, as well as to study more closely the viability and characteristics of the power-law localized and delocalized states suggested there. The work presented in this chapter was published in Eur. Phys. J. B. [35]

## 2.1 Calculation of the Transmission Coefficient $T$ and the Phase Diagram

In this chapter, I realize the original quantum percolation model ($V_{ij} = 0$ for $i$ and $j$ unoccupied) on square lattices of various sizes, and obtain the final average transmission data points $T$ by averaging over several hundred to 1000 disorder realizations for each dilution $q$, energy $E$ and lattice size $L \times L$. The geometry of the system is shown in Fig. 2.1.

The transmission coefficient $T$ was calculated at 6 different energies in the range $0.001 \leq E \leq 1.6$ on 23 to 27 different sizes $L \times L$ depending on $E$, where $10 \leq L \leq 891$. The maximum dilution range was $2\% \leq q \leq 38\%$, with increments of 1% to 5% depending on the simulation batch. Obtaining sufficient data for the phase diagram required multiple batches in which the average transmission coefficient $T$

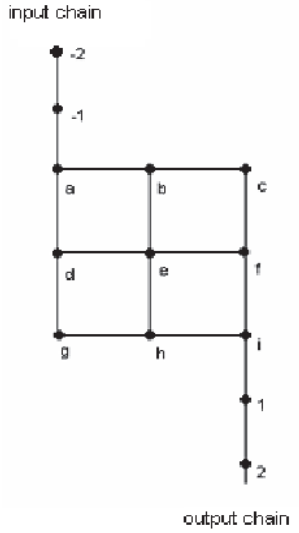


Figure 2.1. Example of a small system of $3 \times 3$ square lattice cluster with a point-to-point connection. The letters label the lattice points of the cluster part of the Hamiltonian, while numbers label those of the leads. The same sequence of labeling is used for all sizes of the clusters in this chapter.

was calculated over successively smaller ranges of dilution $q$ at each energy and lattice size $L$ in order to narrow the location of the transition point, as determined using the procedure summarized below.

A brief note on our choice to study average transmission is in order, especially since the related problem of Anderson localization is sometimes characterized as one where non-self-averaging occurs for certain quantities, in which case the typical value (or geometric mean) of those quantities is preferred over the average. The question of mean versus typical values in quantum percolation has not been commonly discussed; we are aware of only two studies which address the question, neither of which study the transmission coefficient [36, 37].

To determine whether the arithmetic mean ($< T >$) or geometric mean ($e^{<lnT>}$) was most appropriate for our study, we examined the transmission coefficient distribution prior to averaging for a representative selection of parameters; a few examples

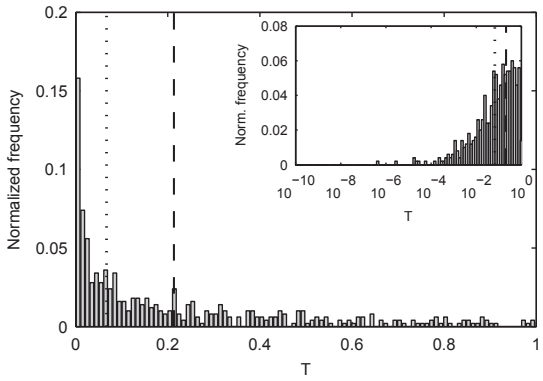


(a)

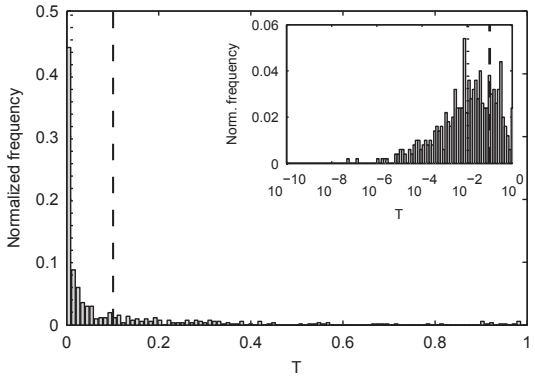


(b)

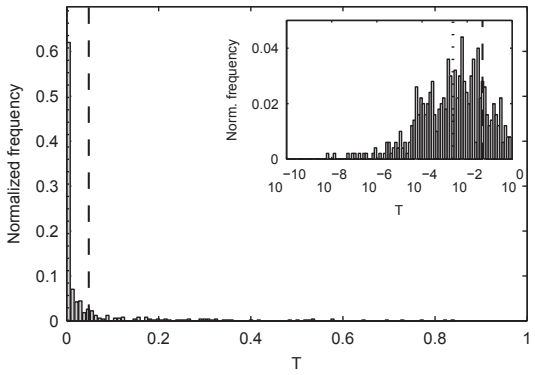


(c)

Figure 2.2. Examples of the histogram of transmission values calculated at energy $E = 1.6$ for (a) $L = 215$ and $q = 0.04$, (b) $L = 215$ and $q = 0.12$, and (c) $L = 624$ and $q = 0.12$ for linear and logarithmic (inset) binning. The vertical dashed line on each histogram indicates the locations of the arithmetic mean (dashed) and geometric mean (dotted) of transmission.

for energy $E = 1.6$ are shown in Fig. 2.2. We see that the shape of the distribution shifts closer toward zero as we increase either dilution (Fig. 2.2(a) vs. Fig. 2.2(b)) or lattice size (Fig. 2.2(b) vs. Fig. 2.2(c)). With linear binning, there is a large peak near $T = 0$, and the geometric mean appears to better reflect this. On the other hand, with logarithmic binning the behavior of the distribution very close to zero is clearer, and we see that while the arithmetic and geometric means are different, both appear to describe the location of the logarithmic bin peak well. Furthermore, we find that the ratio of the two means for a given dilution $q$ stabilizes quickly as $L$ increases, meaning that both averages will show the same qualitative behavior; the presence (or absence) of a delocalized state at a particular $q$ will not be dependent on the type of mean taken. However, as dilution increases past $q \sim O(10\%)$ we begin to find realizations where $T = 0$ (within computing accuracy). Once even a single $T = 0$ realization occurs, the geometric mean is automatically zero, which obscures the fact that all other realizations show transmission to some degree or another, thus leading to a loss of information regarding the localization behavior. This is because the geometric mean is primarily a way of taming rare large values which may significantly alter the behavior of averages, not rare small values; it works well for distributions with long tails stretching out to large values, but in our case $T$ is by definition always between 0 and 1. Due to the loss of information in the geometric mean at mid-to-high dilution, and the fact that both means describe the logarithmic peak well in the low dilution region and have the same qualitative behavior as lattice size increases, we chose the arithmetic mean to be the better quantity to study across our parameter range.

For each energy and dilution studied, the average transmission coefficient $T$ is fitted numerically against lattice size $L$, the best fitting form indicating the localization state of the quantum particle. The quality of the best fits is very good, with the majority having a coefficient of regression $R^2_\sigma \geq 0.98$, and the difference between the best fit $R^2_\sigma$ and that of the other fits is significant with the exception of fits at high dilution as we will discuss below. At lower dilutions the transmission curve was fit in

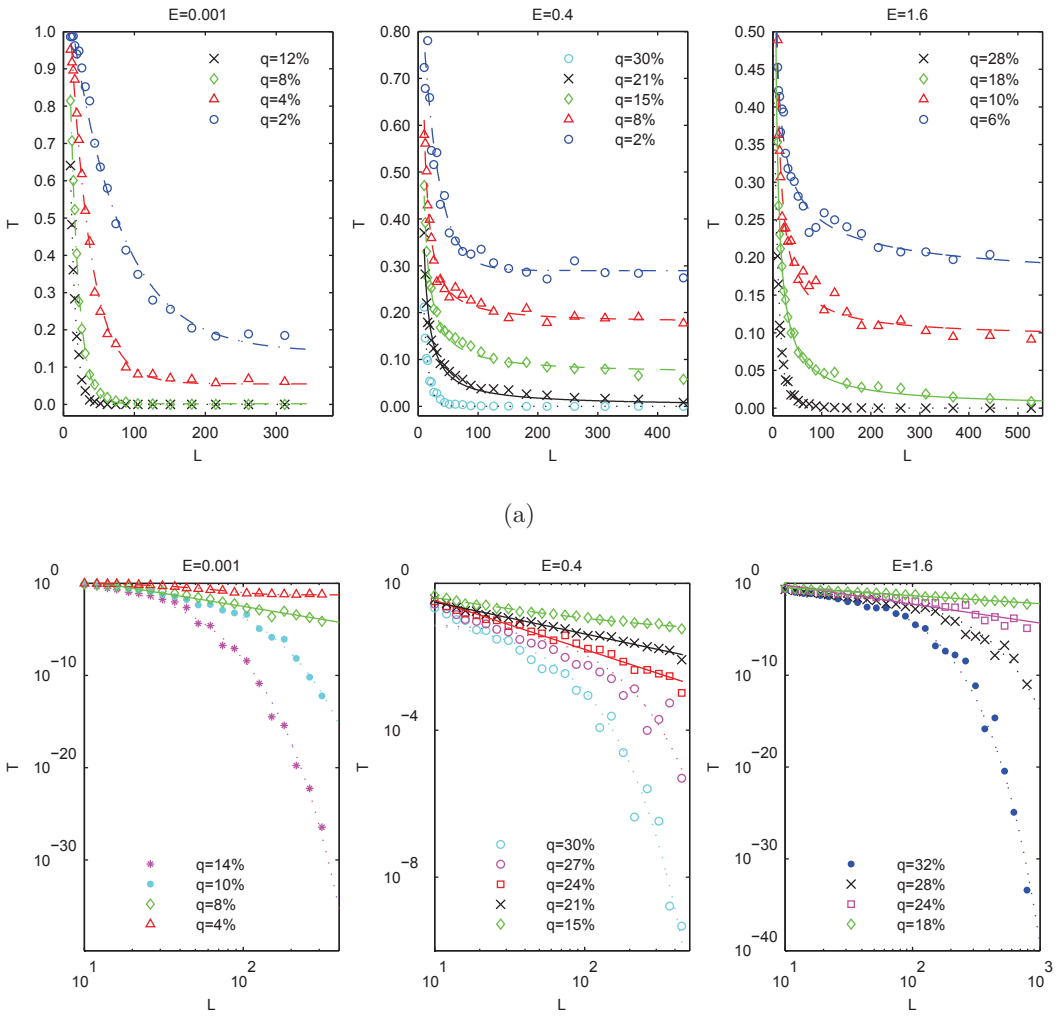


Figure 2.3. Representative transmission curves in (a) linear and (b) log-log scale at 3 energies and various dilutions q. For each energy and dilution, the type of fit determined to be best is shown. An exponential with offset fit (dashed-dotted lines) or power law with offset fit (dashed lines) denotes a delocalized state, power-law fit (solid lines) denotes power-law localization, and pure exponential fit (dotted lines) denotes exponential localization.

linear scale and determining the best fit was straightforward as seen in Fig. 2.3(a). As in Ref. [21], we found that fits denoting delocalization were best at the lowest dilutions (starting at $q = 2\%$), although the type of fit was somewhat different; for low energy, an exponential with offset fit ($T = a\exp(-bL) + c$) gives way to a power law with offset ($T = aL^{-b} + c$) at higher (but still low) dilution, whereas at higher energies the delocalized region is entirely due to a power-law with offset behavior. Likewise in agreement with Ref. [21], we found that the transmission curve becomes best characterized by a power-law ($T = aL^{-b}$) at mid-range dilutions, indicating the particle may be power-law localized, though the locations of the transition from delocalized to power-law localized are somewhat higher than Ref [21] due to our examining a power law with offset fit. Lastly, at the very highest dilutions we found an pure exponential fit of the transmission ($T = a\exp(-L/l)$) to be best, meaning the state is exponentially localized. At all dilutions, we found that the modified exponential fit $T = a\exp(-b(\ln L)^{1/2}))$ proposed by Ziman [31] was not the best fitting form available for any of the parameters studied, even at the energy closest to the band center ($E = 0.001$) and the lowest dilutions we studied (recall that Ziman found this fit to hold true for asymptotically low dilution at the band center on a bipartite lattice).

At high dilutions the distinction between a power-law fit and an exponential fit are generally not conclusive, with each yielding good fits both visually and analytically by looking at the coefficient of regression $R^2_\sigma$ of the two fits. In those cases, we instead fit the transmission curve in a log-log scale, since there is a distinct visual difference between power-law and exponential behavior in that scale. In most cases the switch from power-law behavior to pure exponential behavior as dilution increases was visually apparent; the best fit was determined by using regression coefficients for completeness sake even in those cases, but often visual examination was sufficient. See Fig. 2.3(b) for example. Also important to note is that in log-log scale, the small $L$ portion of an exponential transmission curve looks linear, which necessitated including larger lattice sizes for higher dilutions to increase the certainty that a dilution with a power-law fit really did belong in the power-law localized region and not the

exponentially localized region. There is, of course, a possibility that if still larger lattice sizes were included in the transmission curve, the dilutions which were thought to belong to the power-law localized region would turn out to actually belong in the exponentially localized regime.

The transition point between phase regions was estimated by averaging the upper bound for one state and the lower bound for the other. For example, at $E = 1.6$ the particle is conclusively delocalized for dilutions up to 8% but is conclusively power-law localized beginning at dilutions of 9%, thus the transition point is estimated to be around 8.5%. Narrowing the step size did not always narrow the bounds on the location of the transition point; the state would be conclusively power-law, for instance, up to some dilution $q_p$, then switch back and forth between power-law and exponential for dilutions $q_p < q < q_e$, then be conclusively exponential for all $q > q_e$. In that case the transition point was still estimated as the average of $q_p$ and $q_e$, but associated with a larger uncertainty. Successive batches at the same energy which showed slightly different bounds for the three regions were treated in a similar manner when estimating the overall transition point from those batches used in the proposed phase diagram.

The phase diagram obtained by these calculations is shown in Fig. 2.4; the bipartite nature of the lattice means that the diagram is symmetric about $E = 0$. The results at $E = 0.001$ and $E = 1.6$ agree with our previous work (see, e.g., Islam and Nakanishi [21]) both in the presence of three regions and in the location of the transitions between them. The three regions grow closer together as the energy decreases to the band center, with the power-law region appearing to vanish around $E = 0.001$. If there is a power-law region at this energy, it is very narrow and was not visible in our calculations. However, the delocalized state appears to be always present, suggesting that conduction is possible in this model. These results are consistent with the qualitative phase diagram estimated in Ref. [21].

The presence of delocalized and localized regions with some intermediary region also appears to be consistent with the results of Nazareno et al who studied the binary

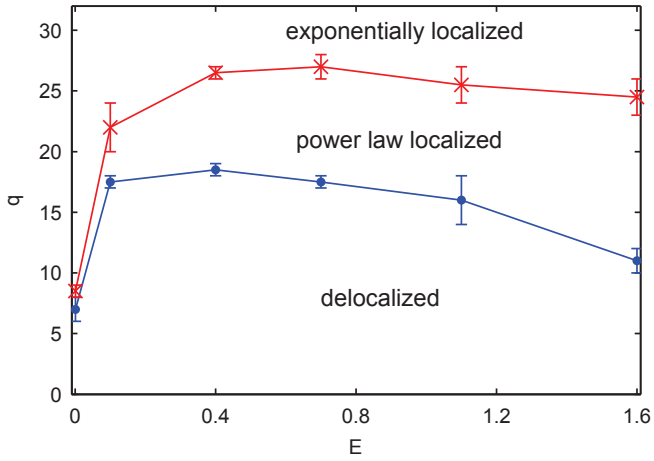


Figure 2.4. Phase diagram for the 2D quantum percolation model with site-based dilution obtained from this work. The presence of the delocalization region at all energies suggests that conduction is possible in this model. The lines between points are included merely to guide the eye.

alloy model (see Fig. 1 in Ref. [18]) in the limit of their variable $\eta \to \infty$; that is, the case when the difference of the on-site energies between two types of sites is very large compared to the hopping term, as in our case of occupied and unoccupied sites. It is also noted that the minimum $q$ for which the exponential localization is observed is rather flat for $E \geq 0.4$, below which it sharply decreases toward the band center ($E = 0$). These observations are in good agreement with the findings of Gong and Tong [22] who used a method centered on von Neumann entropy and also with an earlier work of Koslowski and Niessen [10] who used the sensitivity of eigenvalues to the boundary conditions.

Also, both of the phase boundaries are seen to be non-monotonic with $E$, though the one between the exponentially localized and power-law localized regions is only slightly so. This behavior is consistent with the results of Gong and Tong [22] and we also note that such non-monotonicity had been found by multiple groups for the three-dimensional quantum percolation problem (see, e.g., Soukoulis et al [9]). This type of non-monotonicity is generally due to competing effects that arise when $E$ is

varied. A natural candidate for the competition is between the effect of an increase in the short-range particle diffusivity when $E$ is raised and the very fact that higher short-range diffusivity leads to more interference due to increased scattering from more vacancies at larger lengths.

## 2.2 Analysis of the thermodynamic limit

In order to assess how faithfully our phase diagram represents system behavior in the thermodynamic limit, especially regarding the existence of the delocalized state, we examined how the relevant calculated parameters depend on the fitting region. For the delocalized region, we study the offset term $c$ that appears in the exponential plus offset fits $T \sim a\exp(-bL)+c$ and power law plus offset fits $T \sim aL^{-b}+c$, where a non-zero value indicates the residual transmission as $L \to \infty$. For the power-law localized region, we investigate the power-law exponent $b$ in $T \sim aL^{-b}$. For the exponentially localized region, we focus on the parameter $l^{-1}$ in the fit $T \sim a\exp(-L/l)$, which is the inverse of the localization length $l$.

For each transmission curve (i.e., for a given $E$ and $q$ and varying lattice size $L$), we fit successively larger numbers of points, at first using only the smallest values of $L$ (first 10 for inverse localization length, first 15 for residual transmission and power-law exponent), and then successively adding points corresponding to larger $L$ with each subsequent fit until the entire curve has been used. In all cases the successive fits were done in a linear scale regardless of the dilution, since this yielded the most precise parameter estimates. (While we used a log-log scale for some dilutions to determine the power-law/exponentially-localized boundary in the phase diagram, we found that using that scale when fitting $t$ for those dilutions over successively larger lattices yielded inconsistent behavior for the parameter $b$. Since the log-log scale tends to amplify the behavior of small $L$, we believe it may not be good for precisely determining parameter values, even though it was useful for distinguishing which region of localization the transmission curve belongs in.) At each step, the relevant

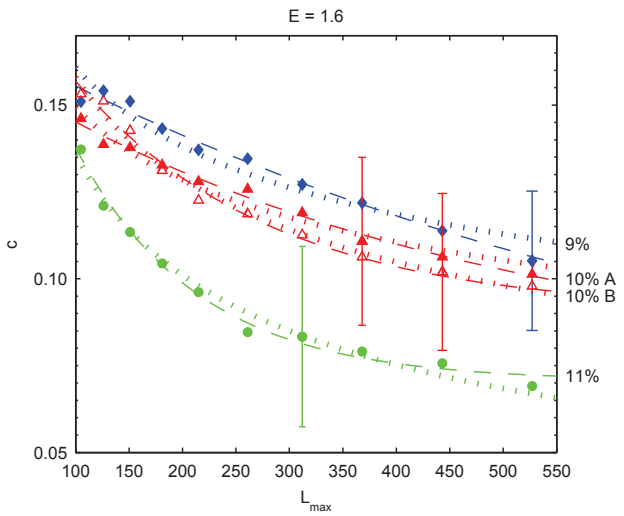


Figure 2.5. For the delocalized region: The estimated offset parameter $c$ is plotted vs. $L_{max}$, the maximum lattice size included in the fit to estimate $c$, for dilutions within the delocalized region at energy $E = 1.6$. In some cases, calculations were based on different simulation batches at the same dilution. Points were further fit with an exponential with offset (dashed line) and with a power-law (dotted line) to determine a limiting estimate $c_\infty$.

parameters ($c$, $b$, or $l^{-1}$) were saved, after which they are plotted against $L_{max}$, the maximum value of $L$ included in the fit, to determine whether the parameters tend toward a stable value ($c_\infty$, $b_\infty$, or $l_\infty^{-1}$) as more points were included and $L_{max} \to \infty$. We take the confidence bounds of the relevant fit parameters ($c$, $b$, or $l^{-1}$) from the successive fitting procedure to be the error bars for those parameters in the plot of ($c$, $b$, or $l^{-1}$) vs $L_{max}$. In general, the error bars decrease for larger $L_{max}$, since adding more points on the transmission curve yields a tighter fit.

For the delocalized region, $c$ does indeed appear to stabilize to a nonzero value. This is illustrated with a typical example from $E = 1.6$ in Fig. 2.5. We further fitted the points in diagrams such as Fig. 2.5 to quantify this stabilization with both another exponential with an offset and a power-law. Both yielded excellent fits, with $R_\sigma^2 \approx 0.98 - 0.99$ in all but a few cases. Although the difference between the quality

of the two fit types was not large, in the majority of the cases the exponential with offset was still the better one. With this type of a fit, in all but a few cases near the phase boundary the limiting value $c_\infty$ excluded zero taking into account the fitting uncertainties. This gives us some confidence that the non-zero transmission persists in the thermodynamic limit. The error bars for $c_\infty$ are determined by fitting the upper and lower bounds of $c$ to extrapolate their value in the thermodynamic limit; that is, the upper and lower bounds of $c_\infty$ are what we would expect to get for the confidence bounds on $c$ for a fit of the entire curve of $T$ vs $L$ with $L \to \infty$. This

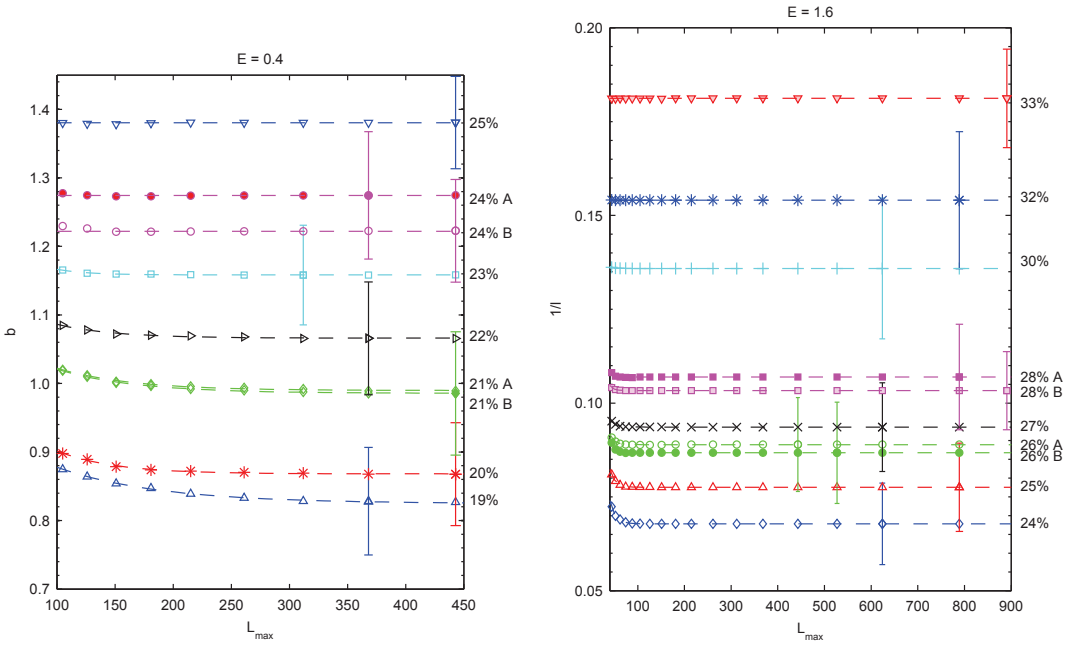


(a) Power law exponent $b$

(b) Inverse localization length $l^{-1}$

Figure 2.6. The relevant parameters are plotted vs. $L_{max}$ similarly to Fig. 2.5, for dilutions within the power-law localized region (a) and the exponentially localized region (b) at representative energies. In some cases, different batches at the same dilution were used. To determine limiting estimates $b_\infty$ and $l_\infty^{-1}$ as $L_{max} \to \infty$, these points were either further fit with an exponential with offset or averaged over all but the first few points before fluctuations dissipated, as shown by the dashed lines.

method is a more generous estimate of the error than choosing the error bars on $c_\infty$ to be the confidence bounds of the $c$ vs $L_{max}$ fit, and more clearly captures the effect on the fit parameter bounds as we increase $L_{max}$ to the thermodynamic limit.

The exponent $b$ of the power-law localized region and the inverse localization length estimates $l^{-1}$ in the exponentially localized region were analyzed in the same manner as the residual transmission $c$ for the delocalized region. The estimates of $b$ and $l^{-1}$ stabilized, in most cases very quickly, as in the examples at $E = 0.4$ and $E = 1.6$ shown in Fig. 2.6. For some dilutions, the parameters were further fitted by another exponential with offset to determine the limiting values $b_\infty$ and $l_\infty^{-1}$, as with an example of $q \leq 23\%$ in Fig. 2.6(a) and $q \leq 26\%$ shown in Fig. 2.6(b). For other dilutions, the fitted data were so flat as to render further fitting impossible (such as the case of $q = 24\%$ and $25\%$ in Fig. 2.6(a), or $q = 30\% - 33\%$ in Fig. 2.6(b)), in which case $b_\infty$ (or $l_\infty^{-1}$) was determined by simply averaging $b$ (or $l^{-1}$) over all but the first few points for which the uncertainty was still decreasing. The resulting estimates of $b_\infty$ increase as the dilution is increased from the delocalized/power-law boundary to the power- law/exponentially localized boundary, and the estimates of $l_\infty^{-1}$ increase as the dilution is increased above the power-law/exponentially localized boundary.

Having obtained the stable values of the relevant parameters for each dilution and energy studied, we next plotted the stable values versus dilution $q$ as shown in Fig. 2.7. In the delocalized region (Fig. 2.7(a)), we see that the residual transmission $c_\infty$ decreases toward the transition to the power-law localized region, as expected. For the energy $E = 0.001$, closest to the band center, $c_\infty$ decreases to nearly zero. For a few dilutions near the phase boundary at other energies (e.g. $q = 16\%$ on the $E = 0.1$ curve) $c_\infty$ may be zero within uncertainty, but the overall trend for energies $E \geq 0.1$ is that $c_\infty$ approaches a finite value at the transition point, suggesting a discontinuity in $c_\infty$ at the transition for that energy range.

In the exponentially localized region (Fig. 2.7(b)) the inverse localization length $l_\infty^{-1}$ decreases as expected in approaching the power-law region. However, it does not appear to decrease to zero, as one would expect for a critical phase transition.

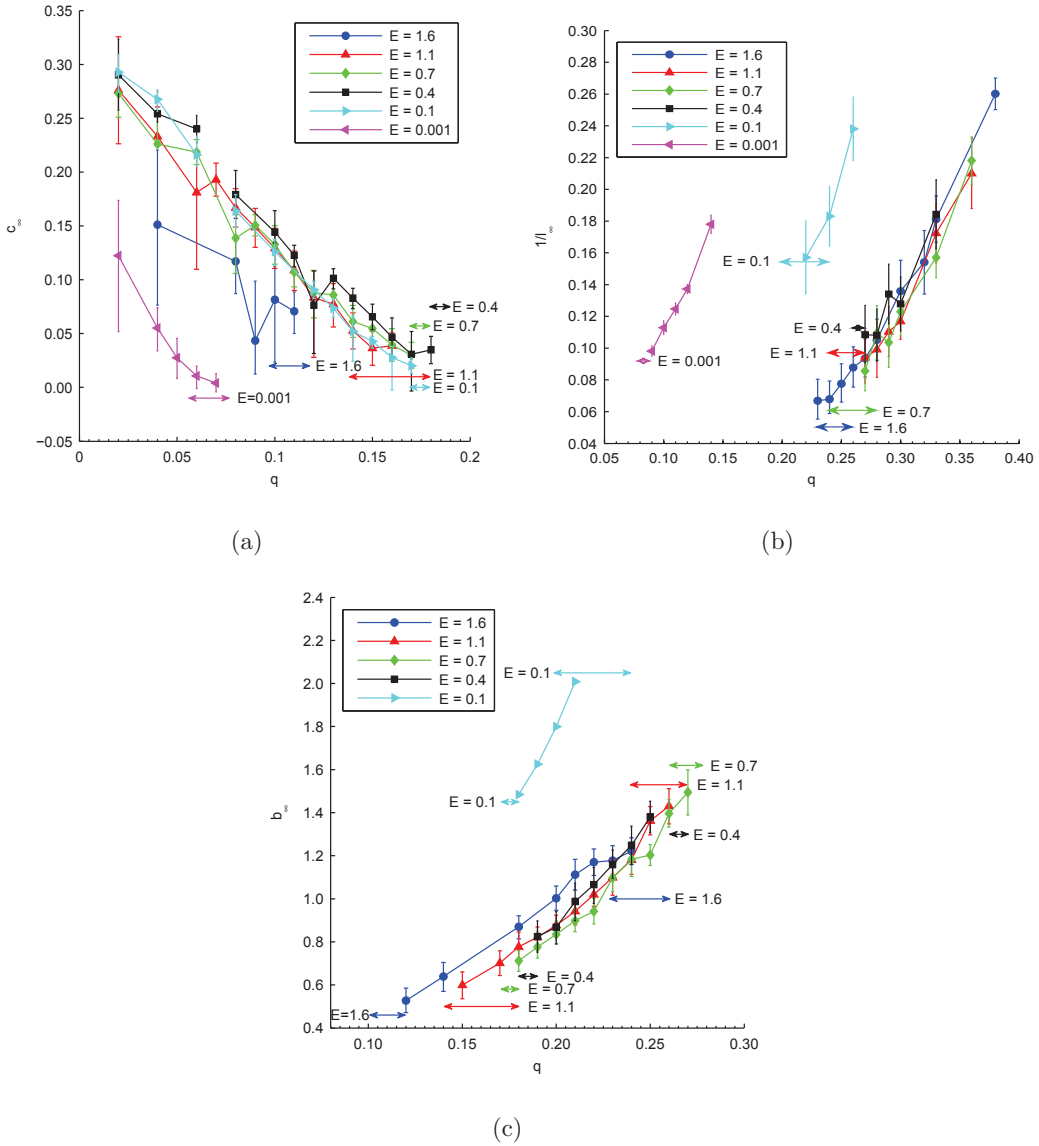


Figure 2.7. The stable values (a) $c_\infty$ of the delocalization offset term, (b) $l_\infty^{-1}$ of the inverse localization length, and (c) $b_\infty$ of the power law exponent are plotted vs the dilution q of the lattice on which they were calculated for all energies studied. In the delocalization case (a), for the lowest three dilutions studied at $E = 0.4$ and $E = 0.1$ and all dilutions at $E = 0.001$ the offset term was from an exponential with offset fit of transmission; in all other cases the term was from a power law plus offset fit. Lines between points are included to guide the eye and are not reflective of any fit. The double arrows denote the transition bounds for each energy as shown in Fig. 2.4.

Rather, at each energy the inverse localization length seems to approach a finite value, possibly suggesting a discontinuity at the exponential/power-law localization transition, which may be reminiscent of the results of recent work on two dimensional melting by Bernard and Krauth [38]. However, we cannot rule out other possibilities such as the transition point simply being overestimated or the $l_\infty^{-1}$ having a non-power-law behavior that only reveals its tendency toward zero extremely near the transition point.

At first glance it is also curious that the $l_\infty^{-1}$ vs $q$ curves for $E \geq 0.4$ all fall nearly on top of each other without any rescaling, while those for $E = 0.1$ and $E = 0.001$ do not. However, this peculiarity may only be a reflection of the fact that the energies $E \geq 0.4$ have very similar values of the transition points $q_c$ and it is possible that $l^{-1}$ mainly depends on $q$ and not as much on $E$. A true, two-variable scaling would be needed to see if data collapsing occurs as in usual critical phenomena and, in that case, it may be possible to also bring in the outlying data from $E = 0.1$ and 0.01 to the same curve.

The curves for the estimated power-law exponents $b$ (Fig. 2.7(c)) for $E \geq 0.4$ likewise all nearly overlap with each other. The exponent appears to vary across the power-law region over a wide range of about 0.2 to 2.0, indicating a non-universal behavior in this region, somewhat reminiscent of below-$T_{KT}$ region of the Kosterlitz-Thouless transition [39].

## 2.3 Summary

We examined quantum percolation on a square lattice with random dilution up to $q = 38\%$ and energy $0.001 \leq E \leq 1.6$ (measured in units of the hopping matrix element), using numerical calculations of the transmission coefficient at a much larger scale than previously. Our results confirmed the previous finding that the two dimensional quantum percolation model exhibits localization-delocalization transitions, where the localized region splits into an exponentially localized region and a

power-law localization region. We determined a fuller, more detailed phase diagram confirming all three regions for energies as low as $E = 0.1$, and the delocalized and exponentially localized regions for energies down to $E = 0.001$. We also examined the scaling behavior of the residual transmission coefficient in the delocalized region, the power law exponent in the power-law localized region, and the localization length in the exponentially localized region. Our results suggest that the residual transmission at the delocalized to power-law localized phase boundary may be discontinuous, and that the localization length is likely not to diverge with a power-law at the exponentially localized to power-law localized phase boundary.

# 3. TWO-DIMENSIONAL QUANTUM PERCOLATION ON ANISOTROPIC LATTICES

Among the various calculations employed to study the quantum percolation model, it stands out that most works based on two-dimensional, highly anisotropic strips yield results supporting one-parameter scaling's prediction of only localized states, whereas our calculations in Chapter 2 and most others finding a delocalized state were based on an isotropic square geometry. One of the studies in the first group was by Soukoulis and Grest, who used the transfer matrix method to determine the localization length $\lambda_M$ of long, thin, quasi-one-dimensional strips of varying width $M$, after which they used finite size scaling to determine the localization length $\lambda$ in the two-dimensional limit and thus the phase of the system.(Ref. [12], see Ref. [40] for more detail on the transfer matrix method in two dimensions) However, they only examined dilutions within the range $0.15 \leq q \leq 0.50$, the lower limit of which is very close to the delocalization phase boundary we found in Chapter 2, which could explain why they did not find any delocalized states. To better understand the differences between our results and theirs, we apply our direct calculation of the transmission coefficient to the quasi-1D scaling geometry used by Soukoulis and Grest over the same energies $E$ and widths $M$ they used, but over a larger range of dilutions extending into lower dilutions than those they examined. We additionally examine the inverse participation ratio of the lattices, which when extrapolated to the thermodynamic limit is another indicator of localization.

## 3.1 Transmision coefficient fits

For this study, we realize the original quantum percolation model on an anisotropic square lattice of varying widths $M$ and lengths $N$ to which we attach semi-infinite

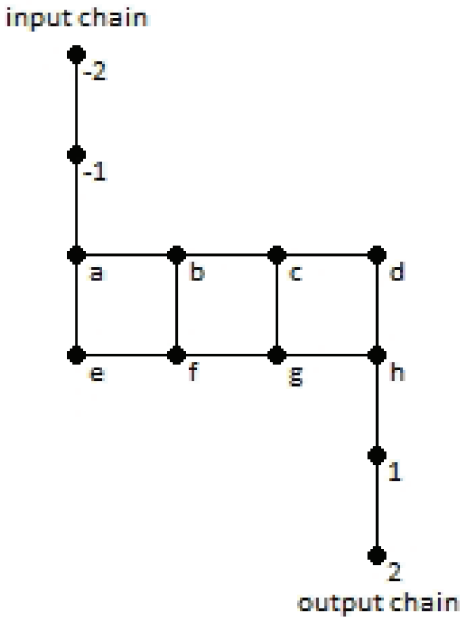


Figure 3.1. A toy example of an anisotropic lattice with input and output leads attached to opposite corners.

input and output leads and which we randomly dilute by removing some fraction $q$ of the sites. $N$ is chosen such that $N = 10 * M$ at minimum to obtain quasi-one-dimensional geometry, and such that it has the same parity as $M$ in order to maintain the symmetry of the bipartite lattice when attaching the leads. We again use a direct solution of the Schrödinger equation (the generalized version of which is given in Eq. 1.11) to calculate the transmission coefficients $T$.

A word about the transmission values is in order here. For these highly anisotropic strips, the transmission is much smaller than for the isotropic square lattices studied in Chapter 2, with the largest $q$ and $N$ having $T = 0$ due to computational underflow. Because of how small the transmission values were for the dilutions and sizes just before the underflow 0s appeared, we wanted to check that the $T$ values were true values, not the result of very small round-off error. The consideration for round-off errors is in part why we measure the transmission coefficients, not the reflection coefficients. Matlab's double-precision floating point variables carry 16 digits of precision for val-

ues as small as roughly 2e-308. Thus if in the solved matrix equation $t < 10^{-16}$, $r$ and thus $R$ would round up to 1 and falsely indicate total reflection, while $t$ would still be represented accurately as some 16-decimal number multiplied by the appropriate factor of 10, as would $T$. Our transmission and reflection calculations for the isotropic lattices of Chapter 2 were, for the most part, large enough to avoid such a round-off in $r$ and $R$ (note in Fig. 2.3b that the smallest $T$ is around $10^{-32}$). However for large $q$ and $N$ on the anisotropic lattices, the transmission decreases to very close to the minimum values able to be represented by floating point numbers, we want to check that they are accurate. To do this, we used Matlab's symbolic mathematics toolbox to solve the Schrödinger equation Eq. 1.11 algebraically to get $T(E, q, M,N)$, from which we could then substitute the appropriate values to get a numeric answer (see Appendix C). This is a very time-intensive calculation and not practical for general use, but allowed us to check a small number of samples. For all cases, the algebraic solution of $T$ yielded values that matched those from our original numerical script given the same parameters. This confirmed to us that the calculated transmissions, while small, are nonetheless accurate.

We calculated the transmission $T$ at the energies $E = 0.05$, 0.25, and 1.05 for anisotropic square lattices of width $M = 8, 16, 32, 64$, and 128 and lengths $N$ within the range $10M \leq N \leq 200M$, and dilutions $2\% \leq q \leq 50\%$. The energies, widths, and dilutions were chosen to match those studied by Ref [12], though additional dilutions $q < 15\%$ were incorporated since our previous work showed a delocalized region at low dilution. The multiples of $N$ were chosen such that the parity of $N$ and $M$ match, to ensure that the input and output leads are on the same sublattice of the bipartite lattices, thus maintaining the symmetry of the resulting phase diagram around $E = 0$. The upper limit of $N$ was determined by computational limitations, since for large $N$ and $q$ the transmission was small enough to result in an underflow 0, as described in the previous paragraph. For most dilutions this occurred for $N \geq 200M$, though for larger energies the cut-off was lower. Despite these computational limitations in calculating $T$, we found that the transmission dropped off with $N$ sufficiently

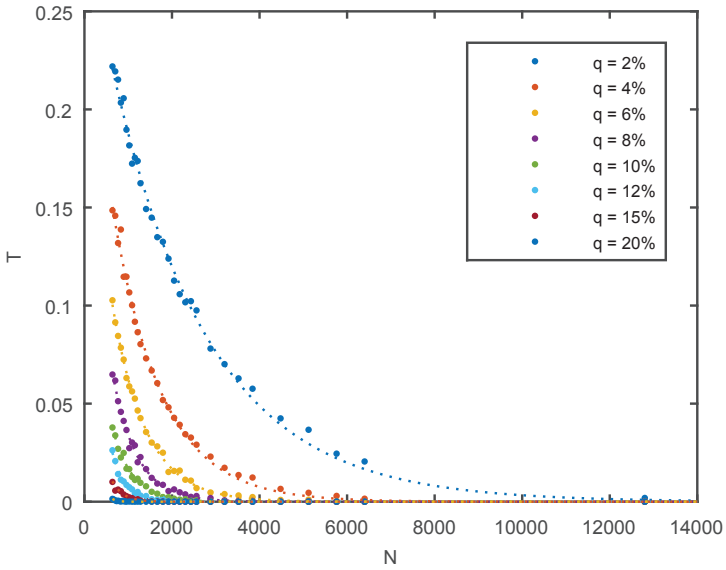


Figure 3.2. Transmission $T$ vs length $N$ for selected dilutions $q$ on lattices with width $M = 64$ and particle energy $E = 1.05$. All transmission curves are shown fitted to an exponential curve (dotted line).

smoothly and quickly that an accurate fit of the transmission was able to be found for all but the highest dilutions ($q \geq 30\%$), all of which fall well above the delocalization-localization phase boundary found in Chapter 2.

Having obtained the transmission coefficients, we then plot transmission $T$ vs lattice length $N$ for each width $M$ and energy $E$, for each dilution $q$ that had a sufficient number of points to establish a fit for the transmission ($2\$ \leq q < leq25\%$ for smaller $M$ and larger $E$). All dilution curves decay exponentially ($T = a*exp(-bN)$), as is to be expected given the highly anisotropic quasi-1D lattices. An example of the fitted $T$ vs $N$ curves for $E = 1.05$ and $M = 64$ at selected dilutions is given in Fig. 3.2. The other ($E$,$M$) pairs have similar transmission curves.

To determine the inverse localization length $b_M = 1/\lambda_M$ in the quasi-one-dimensional thermodynamic limit of a strip of width $M$ and length $N \to \infty$, we use the successive fitting procedure described in Chapter 2 Section 2.2. For each $T$ vs $N$ curve, we fit just the first 6 points, then the first 7 points, etc until all points have been added, saving the parameter $b$ from each exponential fit. We then plot the saved $b$ vs $N_{max}$,

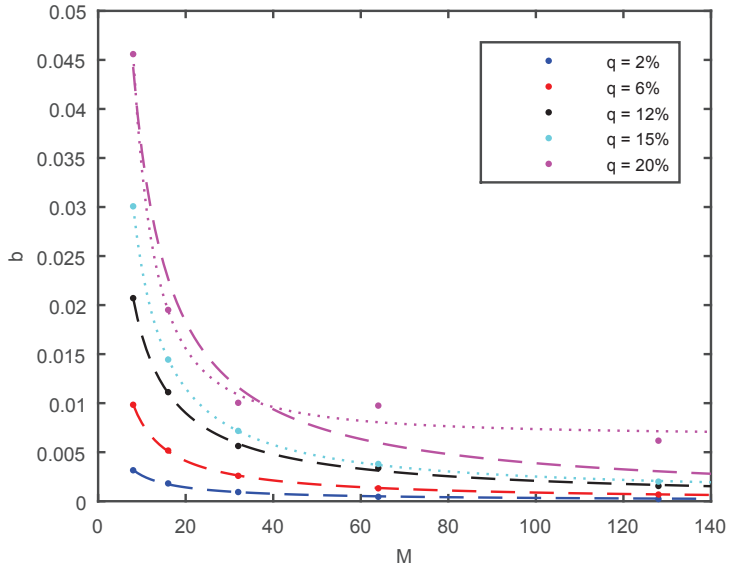


Figure 3.3. Inverse localization length $b_M$ of quasi-1D strips of width $M$ plotted vs. $M$ for selected dilutions $q$ at an energy of $E = 1.05$. At low dilutions the best fit is one which decays to zero, indicating delocalization (dashed line); for higher dilution the best fit is one with an offset term corresponding to the inverse localization length of the systerm (dotted line).

where $N_{max}$ is the maximum length included in the fit resulting in that value of $b$, and fit this new curve to find the non-zero value $b_M$ that the curve stabilizes to as $N_{max} \to \infty$.

Extrapolating $b_M$ to the 2D limit determines the localization of the system: for $b_M \to 0$ ($\lambda_M \to \infty$) as $M \to \infty$, the system is delocalized, but if $b_M \to b_\infty$ ($\lambda_M \to \lambda$) then the system is localized. We fit $b_M$ vs $M$ for each $E$ and $q$ and find that for $E = 1.05$ and $q \leq 12\%$, $E = 0.25$ and $q \leq 15\%$, and $E = 0.05$ and $q \leq 8\%$ , a fit which decays to zero is the best fit, whereas above these dilutions a fit with a constant offset $b_\infty$ fits the $b_M$ vs $M$ curves better, as shown for example at $E = 1.05$ in Fig. 3.3. Thus there *is* in fact a delocalized phase at each energy for these low of disorders. Moreover, while our prior work did not study these energies specifically, the upper bounds for delocalization found here correspond roughly to those found

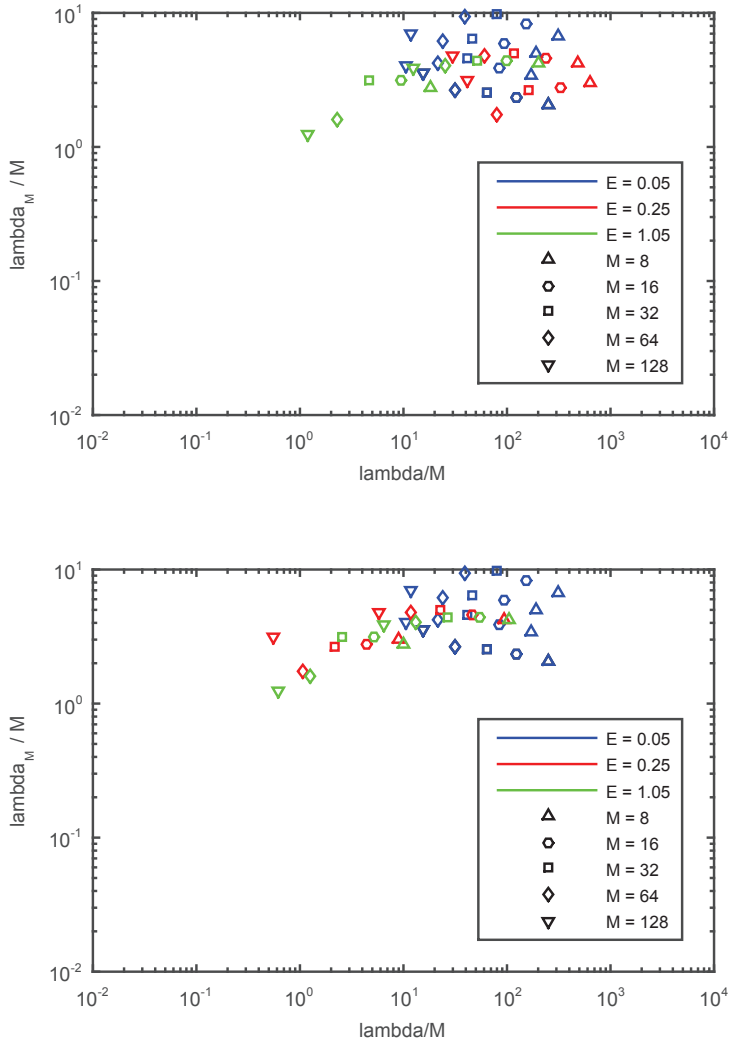


Figure 3.4. Plot of scaled localization lengths $\lambda_M/M$ vs $\lambda/M$ for the widths $M$ (differentiated by marker type) and energies $E$ (differentiated by color) studied. In (a) we use the $\lambda$ extrapolated from the $\lambda_M$ vs $M$ fits, and in (b) we use different values for $\lambda$ at $E = 1.05$ and $E = 0.25$ that fall within the determined error bounds of the extrapolated value.

in Chapter 2; an exact match is not expected due to the different geometry. At the dilutions and energies for which $b_M$ stabilizes to an non-zero value $b_\infty$, we calculate the localization length by $\lambda = 1/b_\infty$.

To most easily compare our results with those of Soukoulis and Grest, we plot $\lambda_M/M$ vs $\lambda/M$ (see Fig. 3.4a) as in their Fig. 1 from Ref. [12]. There are two noticeable differences and one important similarity between their results and ours. First, our figure has no points in the lower left for the smaller values of $\lambda$ and $\lambda_M$. This area is where the small localization lengths at high dilution should be, and their absence is simply a result of the computational limitations of our transmission fit technique, described at the beginning of this section. Secondly, the localization lengths we do have do not exactly overlap in their values with those of Soukoulis and Grest, nor do they all collapse neatly onto one curve. These might partially be explained by a missing factor in our transmission fits; when determining the localization length, we assumed that in the fit $T = a * exp(-b_M N)$, $b_M = 1/\lambda_M$, when it may be that $b_M = c/\lambda_M$, where $c$ is another constant. If there is such a constant, the vertical position of our localization points may be shifted from their true values. Additionally, the $\lambda$ determined by Soukoulis and Grest were a fitting parameter chosen to induce the points to collapse onto one curve, following the scaling procedure outlined in Ref.s [6] and [40], whereas our values of $\lambda_\infty$ were determined independently. Our $\lambda$ do have error bars (omitted from Fig. 3.4 to avoid cluttering the figure) and choosing different $\lambda$ within the bounds of our fit estimates at $E = 1.05$ and $E = 0.25$, for instance, yeilds a better collapse of those energies' localization lengths onto one curve (see Fig. 3.4b).

Despite the differences in our two figures, however, there is one significant similarity. That is, in the dilution range $15\% \leq q \leq 20\%$ for which our work *does* have overlap with the dilutions studied by Soukoulis and Grest, our localization lengths fall within the same order of magnitude of those found by Soukoulis and Grest. They are not precisely the same, but they are not wildly different, either. This gives us confidence that our technique is yielding the same results as theirs, leading us to believe that they simply did not look at small enough dilutions to see a transition, relying instead on an extrapolation that is not in fact correct.

### 3.2 Inverse Participation Ratio calculations

To corroborate our finding delocalized states at small disorder on the anisotropic quasi-1D strips, we also examine the Inverse Participation Ratio (IPR) as the system size increases. We observe that even at the largest and most anisotropic lattice studied, $M = 128, N = 200M$, the IPR distribution of all realizations at small dilution has a distinct peak at $IPR \neq 0$, and the average value is greater than $1/M$, which is the minimum fraction required to span the lattice, whereas at large dilution the peak is near zero (Fig. 3.5). This seems to hint at the transition we observed in Section 3.1. When we plot the average IPR vs N for fixed width (as in Fig. 3.6), we also see that the average IPR decreases much less rapidly than the corresponding transmission T (compare Fig. 3.2), with the IPR at large N remaining well above zero (in fact, the average IPR does not have the problem with computational underflow that the transmission does at large dilution). This illustrates the fact that while the transmission and IPR are related, they do represent different ways of examining localization. It is entirely possible to have many realizations with clusters spanning the lattice that are connected to the input site and to an edge site on the opposite end that is not the output site, as illustrated in the hypothetical example in Fig. 3.7. If this is the case, the average IPR (which is measured over the entire lattice irrespective of the input) would be nonzero while the transmission (which is measured only corner-to-corner) would be very close to zero.

When we fit the average $IPR$ vs $N$ curves at fixed $M$, we observe an interesting trend in the curves as dilution increases. Surprisingly, the $IPR$ vs $N$ at low dilution can be fit very well to a curve with a nonzero offset that we call $IPR_M$. An example at $E = 1.05$ and $M = 64$ is shown in Fig. 3.6 This is unexpected, since in the 1-D limit we know the states are localized, but can be explained as being a result of our including lengths only up to $N = 200M$ due to the computational limitations in $T$. However, as $q$ increases to large disorder, we find that IPR vs $N$ is best fit by a curve decreasing smoothly to zero. This change hints at the phase transition we observed

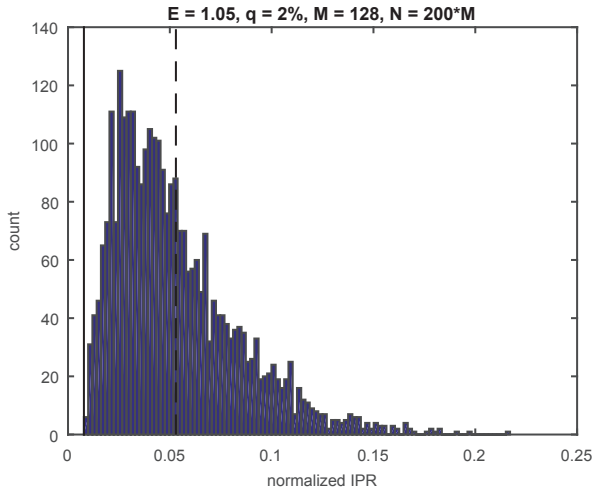


(a)

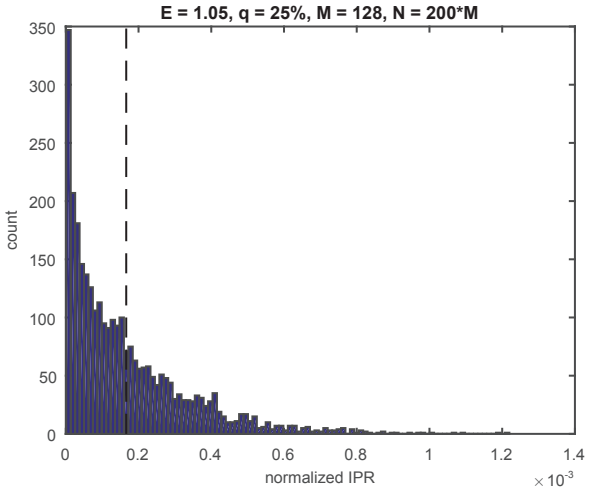


(b)

Figure 3.5. Examples of the histogram of IPR values calculated at energy $E = 1.05$ on a 128x25600 lattice for (a) $q = 2\%$ and (b) $q = 25\%$.The vertical dashed line on each histogram indicates the location of the average IPR for that distribution. For (a), the solid vertical line marks 1/M, which is approximately the lower limit for the IPR required to span the lattice; it is not shown on (b) because it is exceeds the right hand bound of the figure.

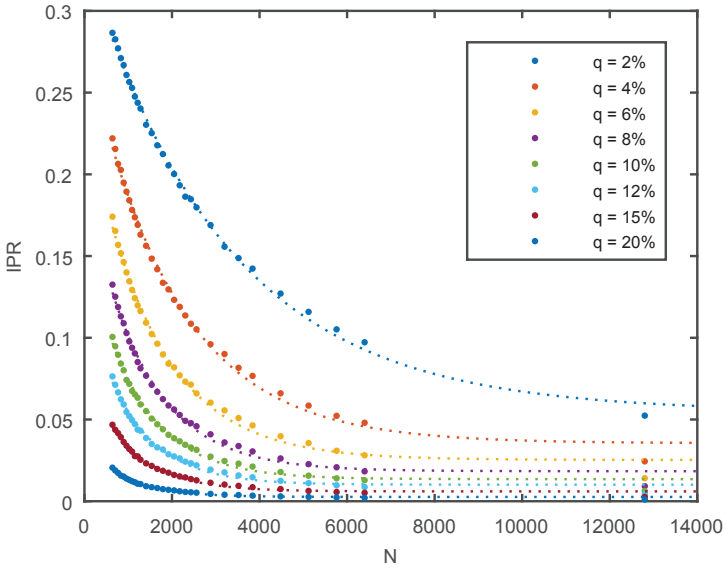


Figure 3.6. Average inverse participation ratio $IPR$ vs length $N$ for selected dilutions $q$ on lattices with width $M = 64$ and particle energy $E = 1.05$, shown fitted to a curve with an offset (dotted line).

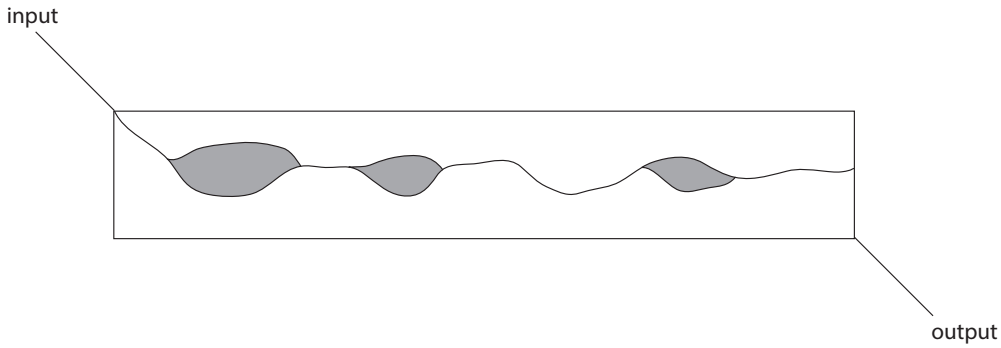


Figure 3.7. An example of a lattice with a connected cluster spanning the lattice but not attached to the output corner.

in the 2D isotropic limit in Section 3.1: if we included still longer lengths N toward the 1-D limit, we should see the $IPR \to 0$ since the 1D limit is purely localized, but if we extrapolate toward an isotropic case, we should see the average IPR approach a finite value for those dilutions at which we found delocalization. To capture the latter situation, we plot the offset terms $IPR_M$ from the lower dilution fits vs $M$

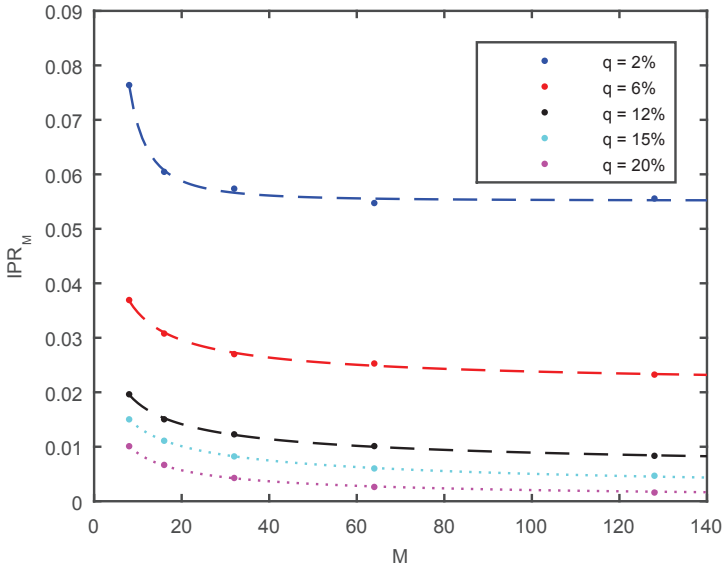


Figure 3.8. Inverse participation ratio $IPR_M$ for fixed-width lattices plotted vs lattice width $M$ for selected dilutions $q$ at energy $E = 1.05$. For low dilution, $IPR_M \to IPR_\infty$ as $M \to \infty$ (dashed lines), indicating delocalization, while at higher dilutions $IPR_M \to 0$, indicating localization (dotted line)

(see Fig. 3.8 for example at $E = 1.05$). Again, we find that at small dilution the $IPR_M$ vs $M$ curve is best fit by a curve with an offset (in this case, a power-law with offset), meaning the IPR grows in proportion to the width and stabilizes to a nonzero fraction of the lattice as we scale toward the isotropic 2D limit. On the other hand, as we increase the dilution, the $IPR_M$ vs $M$ curves eventually are better fit by a pure power law, meaning that although the anisotropic lattices may have had spanning clusters, these clusters do not grow proportionally with $M$ and eventually become disconnected from the output edge, resulting in localization. For $E = 1.05$ this shift to pure power-law fit occurs at $q \geq 15\%$, for $E = 0.25$ at $q \geq 15\%$, and for $E = 0.05$ at $q \geq 8\%$. The results of the IPR study demonstrate that there are spanning clusters in the isotropic limit at low dilution, meaning there are indeed delocalized states at these dilutions, with a transition to a localized state (isolated clusters) at sufficiently high disorder. Moreover, the transition to localized states as disorder increases occurs at

or very near the same dilutions at which we found a transition using the transmission calculations.

### 3.3 Summary

To better understand the difference in our results in Chapter 2 and those based on strip geometry, we applied our direct calculation of the transmission coefficient to highly anisotropic strips of varying widths at three energies and a wide range of dilutions. We find that the localization length of the strips does not converge at low dilution as the strip width increases toward the isotropic limit, indicating the presence of a delocalized state for small disorder. We additionally calculate the inverse participation ratio of the lattices and find that it too signals a phase transition from delocalized to localized states at the same dilutions as those found by the transmission coefficient calculations.

# 4. LOCALIZATION PHASE DIAGRAMS OF TWO-DIMENSIONAL QUANTUM PERCOLATION WITH NON-ZERO BINARY HOPPING INTEGRALS

To investigate what differences in the nature of the disorder between the Anderson model and the quantum percolation model might lead to their differences in transport behavior, we study a modified quantum percolation model in which the binary nature of the quantum percolation models disorder is maintained, while changing the distribution to a finite one that allows tunneling between available and "unavailable" sites. If the infinite-energy aspect of quantum percolation disorder is more important, we expect that changing to a finite energy will result in losing the quantum percolation model's characteristic phases, but not if the binary aspect (which is maintained) is the more important characteristic.

## 4.1 Transmission and localization

In this study, I used the modified quantum percolation model discussed in Chapter 1.4, for which we set $V_{ij} = w$ for $i$ and or $j$ unoccupied, where $0 \leq w \leq 1$ and $w$ is the same for all diluted sites. By doing this, we enable tunneling through and among the diluted sites rather than imposing an infinite energy barrier, while still maintaining a binary disorder. As in previous chapters, we set up the model on a square lattice of varying sizes to which we attach semi-infinite input and output leads at diagonally opposite corners as shown in Fig. 4.1, and use the ansatz proposed by Daboul et al. [17] to calculate the transmission coefficient, with the final data obtained by averaging over anywhere from several hundred to a thousand realizations for each dilution $q$, energy $E$, lattice size $L \times L$, and diluted site hopping energy

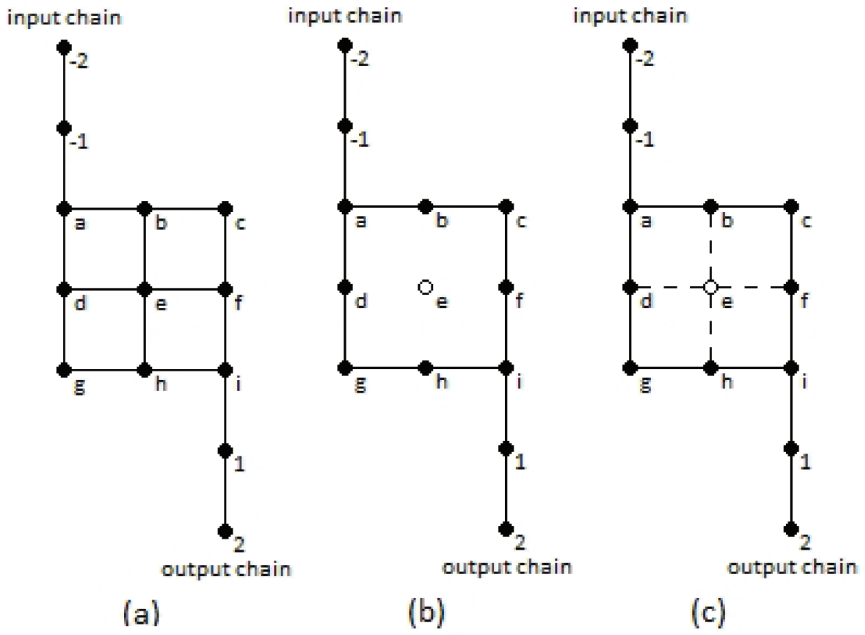


Figure 4.1. Examples of a small system of $3 \times 3$ square lattice cluster with a point-to-point connection. The letters label the lattice points of the cluster part of the Hamiltonian, while numbers label those of the leads. Three types of lattices are shown: (a) a fully-connected, ordered lattice, (b) a diluted lattice in the original quantum percolation model, and (c) a diluted lattice in the modified quantum percolation model studied in this work, with hopping energy $0 \leq w \leq 1$. Lattices (a) and (b) also correspond to the $w = 1$ and $w = 0$ limits of the modified QP model, respectively.

$w$. Significantly, we use an identical set of disorder realizations for every diluted site hopping energy $w$ studied for each choice of ($q$, $E$, $L$); that is, while the initial selection of disorder realizations for each ($q$, $E$, $L$, $w = 0$) is random, all subsequent runs for larger values of $w$ at the same ($q$,$E$,$L$) use the same set of disorder realizations. In doing so, we are essentially taking a set of realizations for the original quantum percolation model at a particular ($q$, $E$, $L$) and slowly "turning on" the diluted site hopping energy from $w = 0$ to $w = 1$ in varying increments. (e.g. in Fig. 4.1, lattices (b) and (c) have the same disorder realization, but in (c) we have "turned on" the

diluted site hopping energy to $w \neq 0$). By duplicating the lattice configurations in this manner, we ensure that any differences in transport that arise are solely due to changing the hopping energy, not to any differences in the disorder realizations chosen, while still selecting a random set of lattices over which to average the transmission coefficient. In order to properly compare the results of the modified model with the original, we calculate the transmission coefficient over the same 6 energies $E$ (in the range $0.001 \leq E \leq 1.6$) and 23 to 27 lattice sizes $L \times L$ depending on $E$ (where $10 \leq L \leq 780$) as were studied in our previous work (Chapter 2, Ref. [35]). The dilution range was $2\% \leq q \leq 50\%$ (slightly larger than before, to account for possible changes within the exponentially localized state above the $q \geq 38\%$ cutoff used previously) and the diluted-site hopping energy was chosen from 23 to 32 values $0 \leq w \leq 1$, both with varying increment sizes.

Before determining the localization behavior of the modified Hamiltonian in detail, we first examined the transmission $T$ vs the diluted-site hopping energy $w$ for a few of the larger lattice sizes for each of the energies. An example of two characteristic energies away from the band center is shown in Fig. 4.2.

There are two notable features to the transmission curves. Most obviously, there is an abrupt change in the transmission between $w = 0.9$ and $w = 1$. Transmission on an ordered lattice has been shown to depend strongly on the energy, with transmission and reflection resonances arising when degenerate eigenstates of the square lattice are split by attaching the semi-infinite leads, resulting in close energies having dramatically different transmission. [41] Thus, it is not surprising that the $w = 1$ limit appears to be a special case. Looking at the transmission for smaller increments of $w$ between $w = 0.9$ and $w = 1$ (see inset in Fig. 4.2) shows wide fluctuations in the transmission between these two values, thus $w = 0.9$ appears to be the lower cut-off for fully-connected-like behavior.

More interesting is the stability of the transmission as $w$ increases. We find that the average fractional cluster size (as measured by simply counting the fraction of sites for which $|\psi|^2 \neq 0$) increases from $S \leq q$ for $w = 0$ to $S = 1$ for $w \geq 10^{-10}$ (the

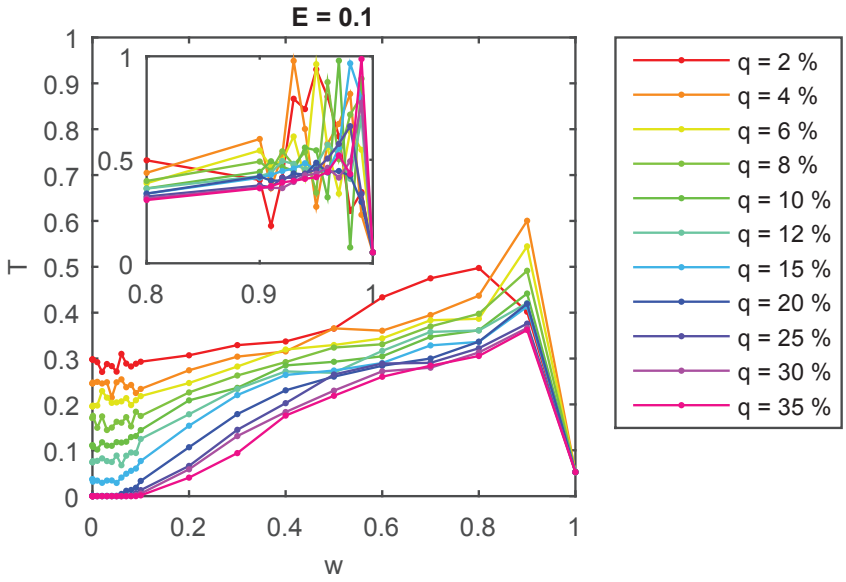


(a)

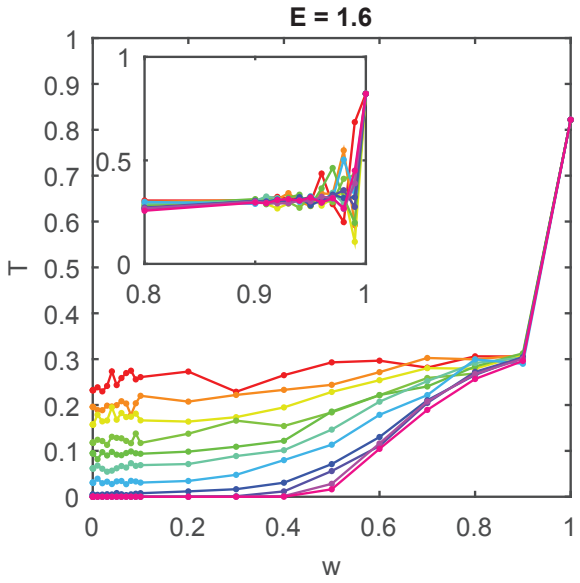


(b)

Figure 4.2. Transmission $T$ vs diluted site hopping energy $w$ on a lattice of size $L = 443$ at various dilutions and the energies (a)$E = 0.1$ and (b) $E = 1.6$, with insets showing a detail of the high-w region with additional points for $w \geq 0.9$. The lines are merely to guide the eye. The abrupt changes in the transmission above $w = 0.9$ and $w = 1$ signals the approach to the fully-connected limit.

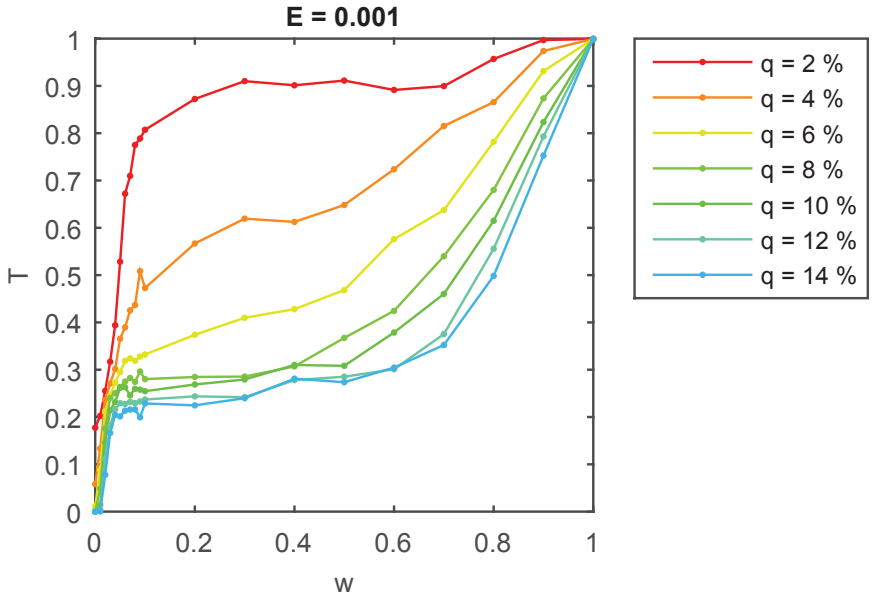


(a)

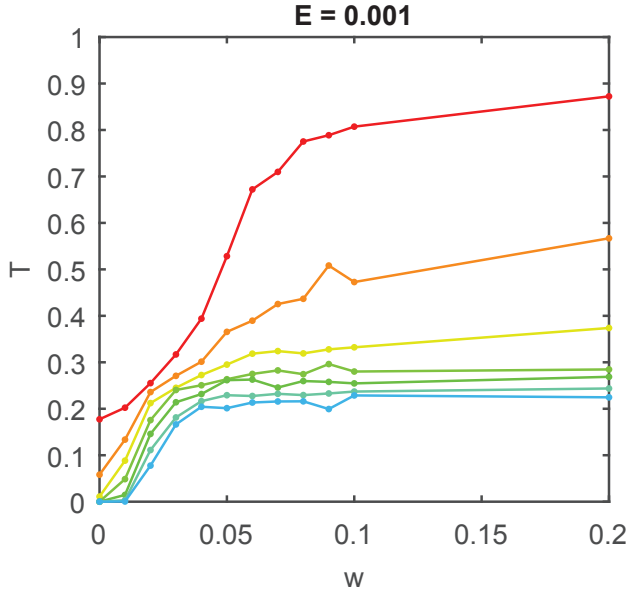


(b)

Figure 4.3. Transmission $T$ vs diluted site hopping energy $w$ on a lattice of size $L = 312$ at various dilutions and energy $E = 0.001$ for (a) the full range of $w$ studied and (b) zoomed in on $w \leq 0.2$ to more clearly show the initial increase in transmission. The lines are merely to guide the eye.

smallest non-zero hopping energy studied), meaning that at least some tunneling occurs for $w \neq 0$. Despite this, the transmission remains stable for up to at least $w = 0.1$ for the smaller energy ($E = 0.1$), and as much as $w = 0.3$ ($E = 1.6$), before it increases monotonically to the maximum transmission at around $w = 0.9$ before the large variations of $T$ set in for larger $w$. Near the band center ($E = 0.001$, Fig. 4.3), the transmission likewise increases monotonically with $w$, but does so much more quickly than at higher energies: for all $q$, the transmission increases rapidly for any $w > 0$. Also unique is the smooth transition to the fully-connected limit.

To construct the complete phase diagram for the modified quantum percolation model, we fit the transmission $T$ vs the lattice size $L$ for each energy $E$, dilution $q$, and diluted-site hopping energy $w$. As in Chapter 2, we find three phases: exponential localization when an exponential fit ($T = a * exp(-bL)$) is best, weaker power-law localization when a power law fit ($T = aL^{-b}$) is best, and delocalization when a fit with an offset (power with offset $T = aL^{-b} + c$ or exponential with offset $T = a * exp(-bL) + c$) is best since $T = c$ at $L \to \infty$. We were unable to satisfactorily fit most transmission curves at $w = 0.9$ due to the variation in transmission upon approaching the fully-connected limit of $w = 1$. However, for all other $w$, the fits were good, with the vast majority of the best fits having ${R_\sigma}^2 \geq 0.95$ and well over half having ${R_\sigma}^2 \geq 0.98$. The fits with lower ${R_\sigma}^2$ occur mostly at very large $w$, where the $T$ vs $L$ curves begin to be less smooth as the system moves more toward the ordered limit with its strong energy dependence, and at the phase boundaries. Additionally, within each phase, the difference between the goodness of the best fit and the next-best fit is significantly distinct. The exception to this are linear-scale fits within the exponentially localized region, in which case we examine curves in the logarithmic scale to distinguish between the two localized fits (as in Ref. [21] and our previous work in Chapter 2/Ref. [35]); and within the power-law region, since any power-law fit can be improved minutely by adding an offset term, in which case the delocalized power-law plus offset fit was only taken to be best if it substantially improved the ${R_\sigma}^2$ compared to a pure power-law fit. For an example at $E = 1.6$ and $q = 30\%$, see

Table 4.1, which lists the ${R_\sigma}^2$ for the possible fits of the transmission curves shown in Fig. 4.4(a), a subset of which are shown with fits in Fig. 4.4(b). As is illustrated in these figures, we find that for each energy $E$ and dilution $q$, the transmission curves progress toward delocalization with increasing residual transmission as the diluted-site hopping energy $w$ increases. For $q$ within the exponentially-localized region at $w = 0$, the system passes through all three phases - exponentially localized, power-law localized, then delocalized - as $w$ increases. If $q$ is within the power law region at $w = 0$, the progression is just from power-law localized to delocalized, and for $q$ delocalized at $w = 0$ system only undergoes an increase in residual transmission.

Table 4.1.
${R_\sigma}^2$ for fits of $T$ vs $L$ at $E = 1.6$ and $q = 30\%$.

| **w** | $T = ae^{-bL}$ (log scale) | $T = aL^{-b}$ (log scale) | $T = ae^{-bL}$ (linear scale) | $T = aL^{-b}$ (linear scale) | $T = aL^{-b} + c$ |
|---|---|---|---|---|---|
| 0 | **0.9819** | 0.7791 | **0.9853** | 0.997 | N/A |
| 0.01 | **0.9876** | 0.794 | **0.9853** | 0.9971 | N/A |
| 0.1 | **0.9854** | 0.9603 | **0.9923** | 0.9983 | N/A |
| 0.2 | **0.9864** | 0.8071 | **0.9925** | 0.9958 | N/A |
| 0.3 | **0.9884** | 0.8313 | **0.9798** | 0.9974 | N/A |
| 0.4 | 0.8539 | **0.938** | 0.9681 | **0.9982** | N/A |
| 0.5 | 0.7898 | **0.9922** | 0.9443 | **0.988** | 0.989 |
| 0.6 | N/A | N/A | 0.5783 | 0.9207 | **0.9757** |
| 0.7 | N/A | N/A | 0.3475 | 0.7403 | **0.9641** |
| 0.8 | N/A | N/A | 0.2925 | 0.6373 | **0.8872** |

The $q$ vs $w$ phase diagrams for the six energies studied are shown in Fig. 4.5. At $w = 0$, the phase boundaries match the phase diagram shown in Fig. 2.4 in Chapter 2 within error bars, including the slight non-monotonicity with respect to $E$. Near the band center, the exponentially localized region seems to vanish for very low $w > 0$.

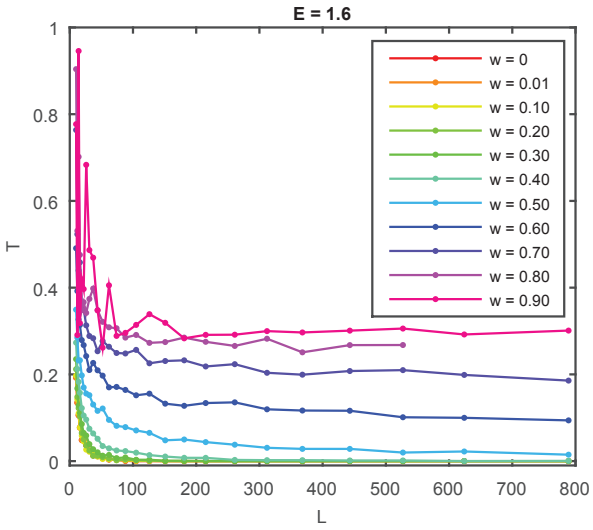


(a)

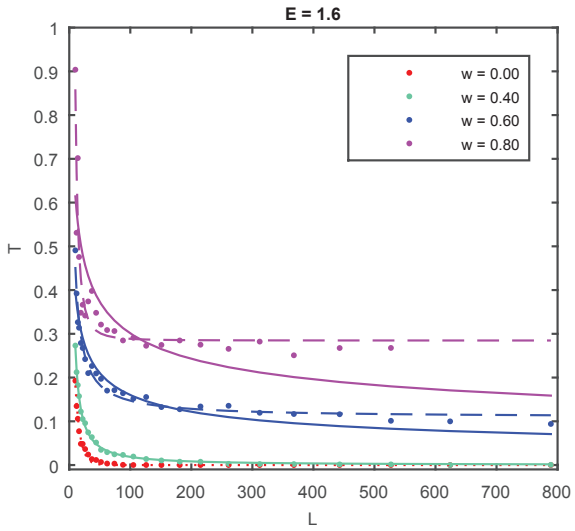


(b)

Figure 4.4. Transmission $T$ vs lattice size $L$ at $E = 1.6$ and q=30% for selected $w$. In (a) the lines connecting the points are to guide the eye; in (b) they are fits (dotted: exponential, solid: power law, dashed: power law with offset) for the transmission curves, which are a subset of the curves without fits shown in (a). In (b), only the best fits for $w = 0.0$ and $w = 0.4$ are shown, while for $w = 0.6$ and $w = 0.8$ the best possible power-law fit for the transmission is included in addition to the actual best fit of a power-law with offset, to illustrate the goodness of the power plus offset fit.

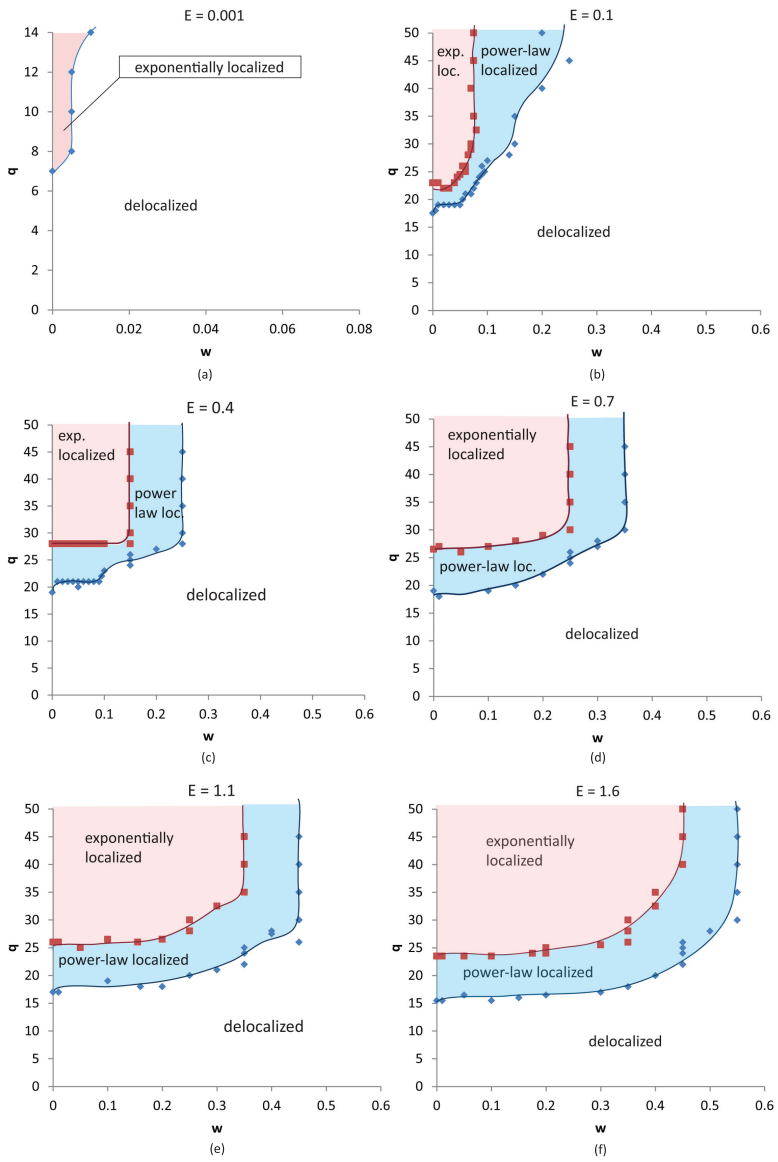


Figure 4.5. Dilution $q$ vs diluted site hopping energy $w$ phase diagram for the 2D modified quantum percolation model at the 6 energies studied ((a) $E = 0.001$, (b) $E = 0.1$, (c) $E = 0.4$, (d) $E = 0.7$ , (e) $E = 1.1$, and (f) $E = 1.6$). The phase boundaries are to guide the eye, not specific fits. We see that for $E \geq 0.1$, the a progressive increase in the size of the three phase regions characteristic of quantum percolation $E = 0.001$ is a special case in which there is no (or vanishingly small) power-law region and the system rapidly becomes delocalized as $w$ increases.

It is possible that for higher dilutions $q$, the exponentially localized region persists to larger $w$, however, we did not study these since calculations at $E = 0.001$ are dramatically more computationally expensive than other energies due to the small diagonal terms making the sparse matrix closer to singular. For all other energies, the phase boundaries between the three regions at fixed $w$ has no quantitative change up to some value $w_{quant}$, with $w_{quant}$ as low as 0.05 for $E = 0.1$ and up to $w_{quant} = 0.35$ for $E = 1.6$. For $w > w_{quant}$, the three regions initially persist with the phase boundaries shifted to higher $q$, but as $w$ increases still further the exponentially localized and then the power law localized regions disappear, leaving all states delocalized at all dilutions. The transitions from three phases to two to only delocalized states each occur at larger $w$ as $E$ increases; there is a progressive increase in the width of the localized phase regions from $E = 0.1$ to $E = 1.6$. For $w = 0.6$ the system is delocalized at all energies as well as at all dilutions. While the non-monotonicity of the phase boundaries as $E$ increases at fixed $w$ can be explained by the competition between interference effects and increased short-range diffusivity described for the original model in Chapter 2.1, we are unsure why localization should persist to higher $w$ as $E$ is increased at fixed $q$, and turn to the inverse participation ratio study described in the next section to explore the localization properties from a different perspective.

The stability of the phase boundaries as $w$ is increased to at least 5% of the available-site hopping energy, combined with the presence of the three phases characteristic of quantum percolation for $w$ up to at least 10% and up to as much as 40% of the maximum $V = 1$ (depending on energy), lead us to conclude that the binary disorder of the quantum percolation model is more significant than the disorder being infinite. Had the latter been more important, we would have expected to see the localized phases vanish much more quickly (if not immediately) upon increasing $w$ from 0 (whereby the infinite energy barriers associated with diluted sites become finite ones).

## 4.2 Inverse Participation Ratio

To help us understand why the transmission (and phase) is initially unaffected by particle's nonzero tunneling probability, we look at the Inverse Participation Ratio (IPR), first at the $w = 0$ limit of the original, unmodified quantum percolation model. For $w = 0$, the maximum IPR is equal to the percentage of available sites $1 - q$; this occurs if the wave function is uniformly distributed over all available sites. In practice, the IPR will be smaller, due to interference effects and the random application of disorder resulting in clusters of theoretically available sites that are disconnected from the main conducting cluster. We examined both the IPR distribution across all realizations and the average IPR on the largest available lattice size in common to all dilutions at a given energy. At $w = 0$, we find that while the average IPR decreases smoothly as $q$ increases, the IPR histogram for the disorder realizations exhibits distinct characteristics depending on the transmission state: for delocalized $q$, the IPR is peaked and looks roughly Gaussian (Fig. 4.6a); for $q$ around and just above the power-law phase boundary, the IPR distribution is more box-like with a tail on the right (Fig. 4.6b); for higher $q$ within the power law region the distribution has a low peak near 0 with a tail (Fig. 4.6c); and for exponentially localized $q$, the IPR is strongly peaked near 0 with a long tail to the right (Fig. 4.6d). Thus the IPR histogram serves as a detailed check on the localization state of the system that is independent of $L$ (because of how we chose to normalize the IPR; see Eq. 1.12).

Visually checking all histograms for all $E$, $q$, and $w$ is obviously cumbersome, so we instead characterize the distribution by its skewness (Eq. 1.13) and kurtosis (Eq. 1.14), which measure the symmetry and shape of the distribution, respectively. We recall that skewness = 0 for a symmetric distribution, while positive or negative skewness indicates a tail on the right or left side respectively, and substantially asymmetrical distributions have $|Sk| > 1$; and that kurtosis = 0 for a normal distribution, negative kurtosis indicates a flat, more uniform distribution, and positive kurtosis indicate a strongly peaked distribution. Combining these two characteristics with our

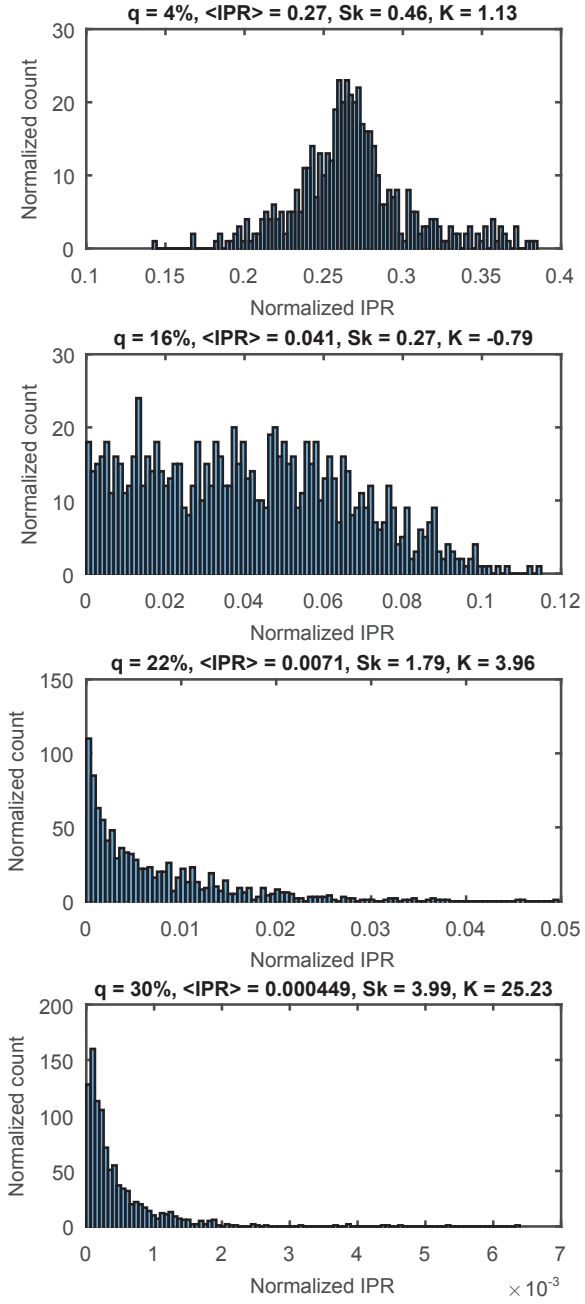


Figure 4.6. Sample of normalized inverse participation ratio (IPR) histograms at $E = 1.6$ and $L = 443$ and $w = 0$ for four different dilutions within (a) the delocalized region, (b) and (c) the power-law localized region, and (c) the exponentially localized region, showing the distributions characteristic of each of those phases. (For $E = 1.6$ phase boundaries are at $q = 15.5 \pm 0.5\%$ and $q = 24 \pm 1.5\%$.)

observations of the histograms in each of the three qualitative phases, we can say that within the delocalized phase $|Sk| < 1$ and $K \approx 0$ (usually roughly $0 \leq K < 1$ because the IPR is slightly more peaked than gaussian in delocalized phase), within the power law region $Sk > 0$ with $K < 0$ at the delocalized-to-power-law boundary moving to $K > 0$ for power-law-to-exponential boundary, and within the exponentially localized phase $Sk > 1$ and $K \gg 1$. Some examples of the IPR average, skewness, and kurtosis are plotted vs dilution $q$ in Fig. 4.7 at $E = 1.6$ and $w = 0$, with the phase boundaries (as determined from the transmission fits) marked. We see that the phase boundaries correspond well with the observed changes in the distribution measures.

We then examine the IPR average, skewness, and kurtosis vs $w$ for different $q$, which reveals a more complex picture with several interesting features. First, for $E \geq 0.4$ (Fig. 4.8), we see that for all dilutions, the average IPR, skewness and kurtosis are all roughly constant for $w \leq 0.1$ except for high $q$ which show fluctuations in the kurtosis. The kurtosis is still within the range indicative of a very sharp peak in the IPR, which for high $q$ (localized states) is near IPR = 0, therefore we do not believe the fluctuations to be indicative of any significant change in the particle's state. Thus for $w \leq 0.1$, the average wave function seems essentially locked in place. While we know that the particle wave function does spread across the entire lattice for $w > 0$ (recall that cluster size = lattice size for $w > 0$), apparently very little of the wave function reaches the newly accessible sites, most likely due to interference effects caused by there still being a strong probability of reflection. Secondly, while the three distinct regions described in the previous paragraph are visible in the IPR average, skewness, and kurtosis combined, the transitions between phases are smooth ones; there are no discontinuous changes in the wave function behavior. As $w$ increases toward the exponential to power-law phase boundary $w_p$ (denoted by square markers in Fig. 4.8) the wave function remains exponentially localized (average near 0, large skewness, and very large kurtosis indicates a strong peak near IPR=0) but on average begins to spread slightly more evenly across the entire lattice including the diluted

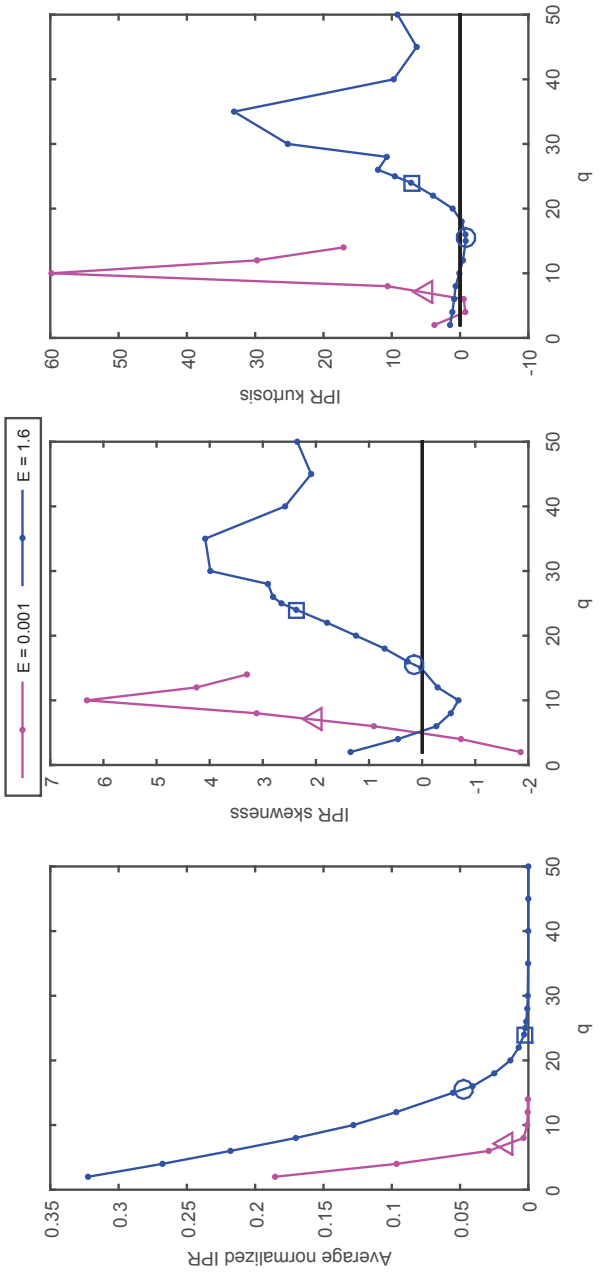


Figure 4.7. IPR average, skewness, and kurtosis vs dilution $q$ for $E = 1.6$ and $E = 0.001$ at $w = 0$, the original QP model. For $E = 1.6$, the delocalized to power-law localized phase boundary and power-law to exponentially localized phase boundary are marked on the curve by circles and squares, respectively; for $E = 0.001$ the phase boundary between delocalized and exponentially localized is denoted by a triangle.

sites (slight increase in average and decrease in kurtosis means fewer realizations with IPR $\approx 0$).

Within the power law region the wave function behavior changes the most: in increasing $w$ from $w_p$ to the power-to-delocalized phase boundary $w_d$ (denoted by circle markers in Fig. 4.8), the wave function continues to spread more evenly across the entire lattice (average IPR increases rapidly) while the system shifts smoothly from being dominated by realizations with the wave function concentrated on a small number of sites (large skewness and kurtosis with smaller IPR) to realizations with a more uniform mixture of participation ratios ($sk \approx 0$ with $k < 0$). (The changes within the power law region are true regardless of whether the system began in the exponentially localized phase or the power-law localized phase for $w = 0$.) Lastly, within the delocalized region ($w > w_d$), the wave function continues to spread more evenly across the entire lattice (average IPR increases), and it becomes more likely that different disorder realizations sustain the wave function over the same number of sites (skewness and kurtosis indicate a shift from a low peak to a tight peak).

For $E = 0.1$ and $q \geq 18\%$, the IPR distribution (as described by the average, skewness, and kurtosis) is much the same as for $E \geq 0.4$, the primary exception being that the distribution remains stable from $w = 0$ only up to $w = 0.05$, not to $w = 0.1$ (Fig. 4.9). However, for $q < 18\%$, i.e. dilutions for which the state is delocalized for all $w$, there is a curious drop in the average IPR around $w = 0.1$ that is not accompanied by a similar drop in the transmission, which is roughly constant over this range (compare Fig. 4.2). The trend of the skewness and kurtosis of the IPR distribution at $E = 0.1$ are not very different from the other energies (the phase shifts occur at lower $w$ as given by the phase diagram Fig. 4.5b, but the shape is the same), so it seems the change is only in the average IPR, not in the shape of the distribution. The dip around $w = 0.1$ occurs for all lattice sizes, making it less likely that it is a finite size effect. While we are not certain what could be causing such (apparently) anomalous behavior, our best estimate is again that interference effects are at play: it is conceivable that increasing the hopping energy temporarily increases

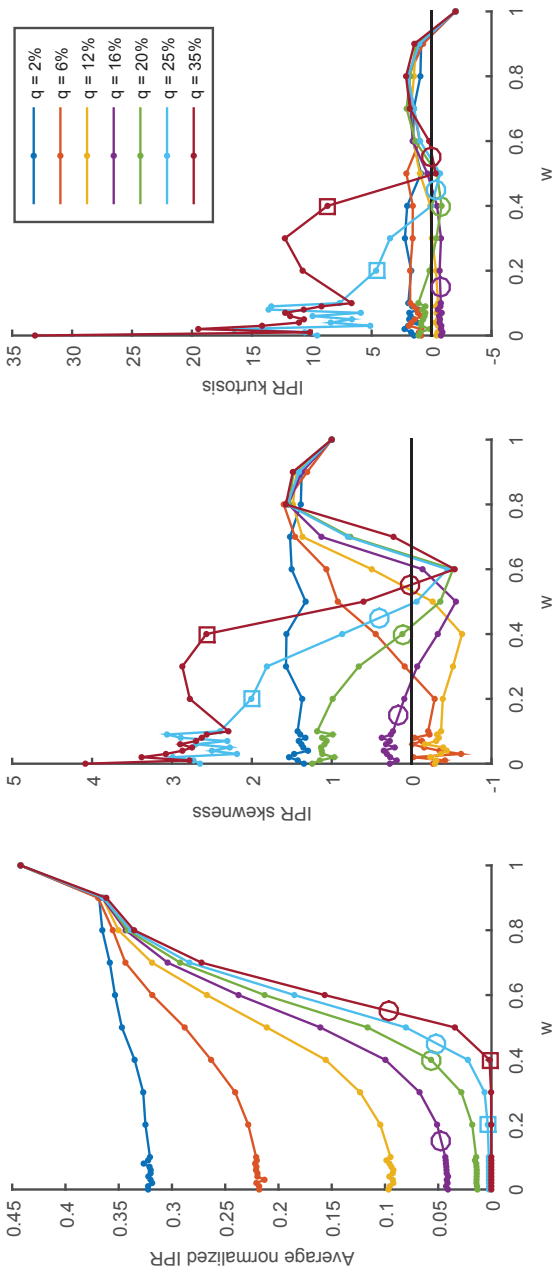


Figure 4.8. IPR average, skewness, and kurtosis vs diluted site hopping energy $w$ for $E = 1.6$ at selected dilutions. The exponential to power law localization phase boundary and power law to delocalized phase boundary are denoted on each curve by squares and circles, respectively. If a curve has no markers, it is in the delocalized phase for all $w$; if it only has one marker, it begins in the power-law localized phase at $w = 0$ and shifts into the delocalized phase.

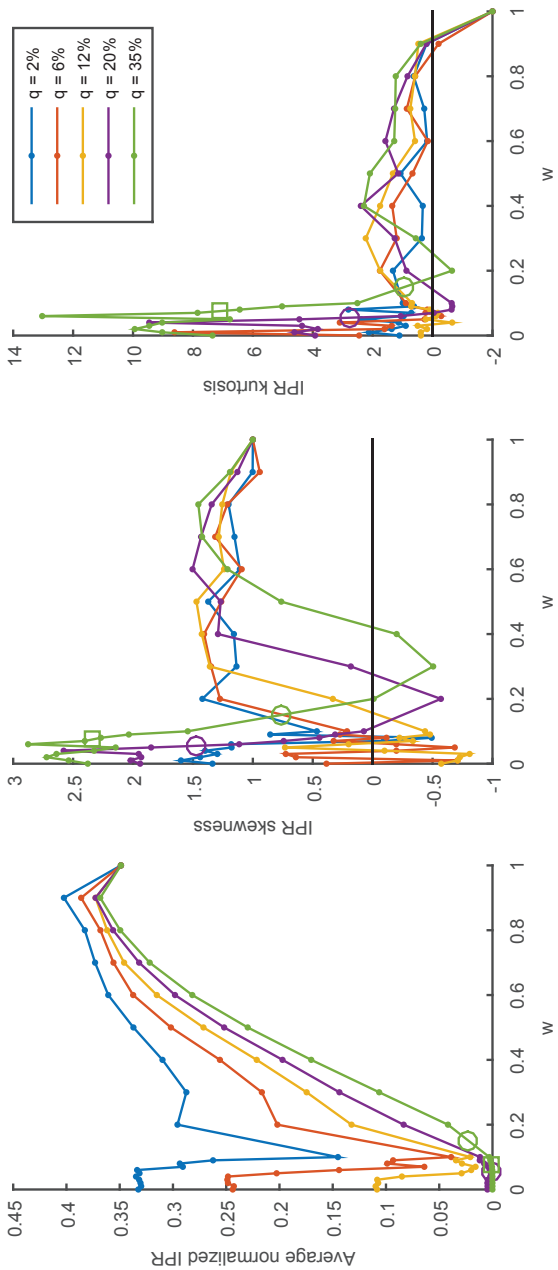


Figure 4.9. IPR average, skewness, and kurtosis vs diluted site hopping energy $w$ for $E = 0.1$ at selected dilutions. The phase boundaries are marked on each curve as in Fig. 4.8. We see that there is an anomalous dip in the average IPR of initially delocalized $q$ for small $w$.

the probability of destructive interference on sites that had always been available, thereby constraining the wave function to a narrower path while sustaining the same transmission, before a further increase of $w$ begins to overcome such interference effects and IPR rises.

For $E = 0.001$, the energy nearest to the band center, we see even more interesting and unexpected behavior. It is not entirely unexpected that states very close to the band center behave differently, as several studies have shown $E = 0$ to have unique characteristics in quantum percolation. [20, 31, 42] However, it is peculiar that at this energy the IPR increases more slowly than the transmission does, in contrast to all other energies, at which the IPR and transmission increase at a similar rate. Apparently, the wave function is constrained to a very narrow selection of sites even at low $q$, so increasing the hopping energy of the diluted sites along that path reduces the destructive interference they cause, thus significantly increasing the transmission even as the transmitting cluster remains roughly the same size. This is consistent with our knowledge that for quantum percolation, the eigenstates of $E = 0$ are dominated by many states with small spatial extent, leading to lower transmission and localization at smaller $q$ in the original model. [8] Our work examines a continuous spectrum in which the particle wave function is a mixed state, but it is reasonable to believe the mixed state to be similarly dominated by small spatial clusters. More unusual is that for $q = 2\% - 6\%$ (for which the system is delocalized for all $w$), we again see an unexpected drop in IPR just above $w = 0$, where there is no such drop in the transmission (see inset on Fig. 4.10). In this case, due to the increments in $w$ studied, it is highly probable that there is actually a singularity in the average IPR at $w = 0$; regardless, the behavior is still puzzling. Furthermore, for $w \leq 0.15$, the relationship between IPR and $q$ is inverse of what we would expect (and inverse of the relationship between transmission and $q$), that is, we see the smaller dilutions having the lower IPR, meaning the wave function is more tightly constrained in the lattice at lower dilutions than at higher ones.

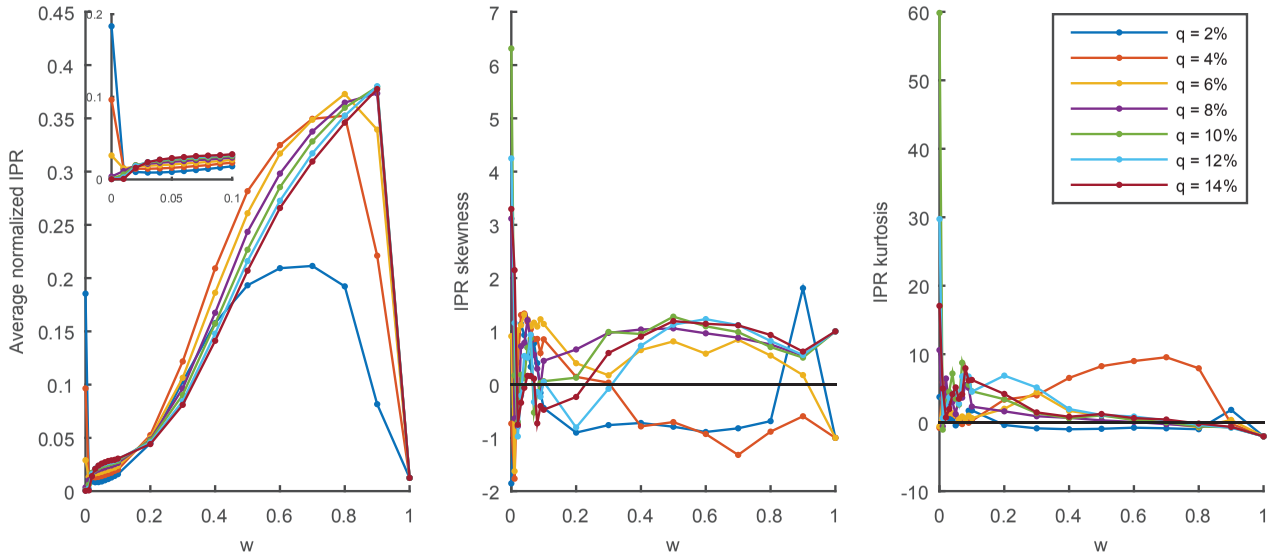


Figure 4.10. IPR average, skewness, and kurtosis vs diluted site hopping energy $w$ for $E = 0.001$ at selected dilutions. The phase transitions are not marked on these curves; for $q \geq 8\%$ there is a transition from exponentially localized to delocalized at $w = 0.005$. For the initially delocalized $q$ there is a drop in the average IPR above $w = 0$ (see inset), similar to that seen at $E = 0.1$. For all dilutions, below $w = 0.2$ the relationship between IPR and $q$ is inverse of what we would expect, with the lower dilutions having a lower, not higher, IPR.

## 4.3 Summary

We studied a variation on quantum percolation in which the hopping integral ($w$) associated with bonds that connect to at least one diluted site is not zero, but rather a fraction of the hopping integral (V=1) between non-diluted sites, by calculating transmission coefficient and the inverse participation ratio. We find the original quantum percolation results to be stable for $w > 0$ over a wide range of energy. In particular, except in the immediate neighborhood of the band center (where increasing $w$ to just $0.02 * V$ appears to eliminate localization effects), increasing $w$ only shifts the boundaries between the 3 regimes but does not eliminate them until $w$ reaches 10%-40% of $V$. This suggests that the binary disorder of the quantum percolation model is more significant than the disorder being infinite. Additionally, the IPR distribution indicates that very little tunneling occurs for $w < 0.1$ for $E \geq 0.1$, while for $w > 0.1$ the particle's wave function gradually tunnels more and more through the newly accessible diluted sites, smoothly spreading across the lattice as $w$ increases. We also find a few anomalous trends in the IPR at small $E$.

# 5. ANALYSIS AND CONCLUSIONS

## 5.1 Phase diagram of original quantum percolation model

We first examined the original quantum percolation model on randomly diluted square lattices of size $L \times L$, for which we calculate the transmission coefficient and related quantities numerically and analyze the results by methods such as finite-size scaling. Our analysis indicates that, at all energies except possibly very near $E = 0$, the quantum percolation model in two dimensions possesses delocalized, power-law localized, and exponentially localized regions. The power-law region becomes narrower as the energy approaches the band center, and possibly disappears there. This is consistent with our group's previous more limited-scale work [21], but the current work covers a wider parameter space, uses larger lattice sizes $L$, and has better statistics, allowing systematic extrapolations to the thermodynamic limit. Various aspects of our findings are also consistent with other previous works such as Ref. [17, 19, 22].

Additionally, the inverse localization length extrapolates to non-zero limits as system size $L \to \infty$ in the exponentially localized region, and the residual transmission coefficient extrapolates to a non-zero limit as well in the delocalized region, as appropriate. However, the localization length does not appear to diverge as the dilution $q$ approaches the phase boundary with the power-law region, and (with the exception of $E = 0.001$) the transmission coefficient does not seem to decrease all the way to zero at the delocalization-localization boundary.

At this stage, we cannot make any firm conclusions regarding the precise nature of the transitions which were observed numerically. However, Schuster [43] proposed an analogy of the Anderson localization problem to a dirty XY model (mentioned also in Abrahams et al [1]), which leads us to speculate whether there is also a connection

with the quantum percolation model. The discontinuous change of transmission $T$ at the delocalized-power-law transition is reminiscent of the discontinuity in the superfluid density of two-dimensional superfluid transition or the helicity modulus in the 2D XY model at the Kosterlitz-Thouless transition [39], both of which are continuous transitions. The transmittance in our problem is, like the superfluid density and the helicity modulus, a response function, and thus its discontinuity at the delocalized to power- law localized transition is consistent with a continuous transition. Such an analogy clearly remains speculative at this point until a suitable order parameter in quantum percolation is identified and directly compared.

At the other boundary, the power-law to exponentially localized transition, the seeming discontinuity of the inverse localization length $l^{-1}$ could be an indication that this transition is of first order, but it could also be a reflection of a difficulty in estimating the boundary accurately or of a non-power-law nature of the divergence of the localization length there. As an example of a correlation length that diverges by a non-power law, we cite the exponential behavior ($\xi \sim exp\left[a\left(\Delta T\right)^{-1/2}\right]$) of the Kosterlitz-Thouless problem, approaching the transition from $T > T_{KT}$. The fact that many previous works which attempted to estimate this exponent came up with values that differ over an order of magnitude from $O(0.1)$ to $O(1)$ (compare, e.g., the values reported in Ref. [22] and [17]) is suggestive that this transition is not yet fully understood. It is also intriguing that Soukoulis and Grest [12], while concluding that the delocalization is possible only at $q = 0\%$, obtained a numerical result where $\xi \sim exp\left[a\left(\frac{p}{1-p}\right)^{1/2}\right]$ where $p$ is the occupied fraction, a complement of our dilution variable $q$.

Considering the two transitions together, our results may raise yet another speculation of an analogy to the two-step transition [44] of two-dimensional melting with the intermediate hexatic phase. The latter exhibits a power-law translational correlation in the solid phase, only a power-law orientational correlation in a hexatic phase, and exponentially decaying correlations in the liquid phase [38,44]. Although the theory of these transitions indicate both solid-hexatic and hexatic-liquid transitions to

be of continuous, Kosterlitz-Thouless type, there are some recent experimental claims that the latter transition is discontinuous [38]. However, obviously further work is needed to characterize the observed transitions more accurately.

## 5.2 Percolation on anisotripic lattices

We next studied the quantum percolation model on highly anisotropic two-dimensional lattices, scaling toward the isotropic two-dimensional case (studied in the previous chapter) to determine the localization state and localization length in the thermodynamic limit. We determined the localization length by a two-step process in which we first determined the inverse localization length $b_M = \lambda_M$ of the anisotropic strips, then extrapolated the localization length $\lambda$ of the isotropic system from the trend of the $b_M$ as $M \to \infty$. Although the transmission calculations only allow us to study a limited range of dilutions effectively due to computational limitations, we nonetheless were able to detect a phase transition at specific dilutions, above which the M-width strip inverse localization lengths $b_M$ converged to a finite value, and below which they decayed to zero, indicating an infinite, lattice-spanning extended state. The location of the phase transitions are consistent with the phase boundaries found in Chapter 2, but their existence is in contradiction to the results predicted by Soukoulis and Grest in their transfer-matrix method studies of quantum percolation. [12] This contradiction can be resolved by observing that they only studied dilutions above $q = 15\%$, which is above the delocalization-localization phase boundary found in this and the previous chapter. The localization lengths found in this chapter for dilutions within the localized region fall within the same order of magnitude of those found by Soukoulis and Grest at the lower end of the range of dilutions they studied, leading us to believe that they simply did not look at small enough dilutions, thus missing the phase transition.

We additionally checked the localization state of the system by studying the inverse participation ratio of the lattices, which tells us what fraction of sites sustain

the particle wave function. We find that even on narrow anisotropic strips, at small dilution the average IPR shows a distinct peak away from zero at a value large enough to span the lattice, while at large dilutions the peak is near zero. When we scale toward the isotropic limit, we find that the IPR vanishes for large dilution, indicative of localization, while it approaches a finite value for low dilution, indicative of a delocalized state. Furthermore, the dilutions above which the inverse participation ratio vanishes in the isotropic limit match the phase boundaries found in the first part of the chapter.

The results of our work in this chapter serve two purposes. First, by using the same basic technique (transmission coefficient and inverse participation ratio measurements) as our previous work on a different geometry - that is, highly anisotropic lattices scaled to the 2D thermodynamic limit - we obtain the same delocalization-localization phase boundary results, showing that the phase transition found previously was not dependent on our using an isotropic geometry. Secondly, by using the same geometry as Soukoulis and Grest, we found overlap between our localization length results and theirs at higher dilutions, but also examined smaller dilutions and found a delocalized state, leading us to believe that they incorrectly assumed they could extrapolate their results from $15\% \leq q \leq 50\%$ toward even smaller dilutions. Had our localization lengths within their range dramatically differed from theirs, we would perhaps conclude that the differing techniques used led to the difference in whether a delocalized state was found, but as we have shown, this is not the case.

### 5.3 Modified quantum percolation with non-zero hopping integrals

Lastly, we studied a modified version of the quantum percolation model in which the diluted site hopping integrals are allowed to be non-zero, thus introducing the possibility of tunneling through and among the previously inaccessible diluted sites while maintaining a binary disorder. Using the same transmission curve fitting technique as the first chapter, we determined a full three-parameter phase diagram showing

the effects of changing the diluted site hopping energy along with the dilution and particle energy. From these phase diagrams, we see that the quantum percolation model is a surprisingly robust one, with the three phases characteristic of the original model persisting to at least $w = 0.05$ for $E \geq 0.1$, and to even higher $w$ for larger $E$. By examining the average inverse participation ratio, we see that in fact, for $w < 0.05$ to 0.1, the modified model shows results that are nearly identical to the original even as far as the individual realizations, with the wave function being predominately constrained to the original (undiluted) sites despite a small fraction of the wave function tunneling to and through the now-accessible diluted sites. For these very small $w$, then, there are still strong interference effects that continue to work in conjunction with the underlying disorder to cause localization. At higher values of $w$, the wave function is able to spread more evenly across the entire lattice, but it is not until $w \simeq 0.6$, a surprisingly large hopping integral, that the wave function is delocalized for all energies $E$. Thus, we see that for lower $w$, the modified quantum percolation model is dominated by the amount of disorder $q$; though interference effects are weakened as the hopping integral increases, it is not enough to affect localization character. Since the quantitative and then qualitative characteristics of the original quantum percolation model are maintained for such a wide range of diluted site hopping integral, we conclude that the binary nature of the disorder is the defining characteristic of the QP model, not the existence of infinite-energy barrier. Finally, at sufficiently high $w$, the phase behavior is dominated more by the diluted site hopping integral than the amount of disorder $q$ present, evidenced by the vertical phase boundaries for the localized states.

The energy nearest the band center is the exception to the rule. In this case, we find that increasing the diluted site hopping integral quickly moves the system into the delocalized phase for all $q$. Furthermore, the increased transmission corresponding to the phase change is not accompanied by a commensurate change in the IPR, which remains very small and does not increase dramatically until $w > 0.2$. It may be possible to interpret these two results combined as reflecting the fact that the wave

functions are constrained to a large number of small spatial clusters at the band center for a wide range of $q$, and thus an increase in $w$ has a large effect on suddenly creating a connected path through the lattice for the quantum particle, while it has a much smaller effect on creating a large cluster on which the wave functions can reside. We additionally observed a singularity in the IPR at $w = 0$ for low $q$ corresponding to the delocalized region, and an unexpected inverse relationship between IPR and dilution for $w < 0.2$. Further study will be needed to interpret these two points more clearly, although the overall results are consistent with the band center having special characteristics in the quantum percolation model.

We also observed an anomalous decrease in the IPR for $E = 0.1$ at lower dilutions for which the system is always in the delocalized phase. The anomaly only occurs in the average IPR; the shape of the distribution of IPR realizations appears unaffected, as is the transmission. We are unsure of what causes this anomaly, or whether it is of significance since it does not affect the overall phase of the system.

In conclusion, we have seen that the quantum percolation model is a robust and complex one. That the model remains quantitatively unchanged for a range of $w \neq 0$ broadens its applicability to materials and systems in which it is unrealistic for impurities to be modeled as completely isolated from the rest of the material. Additionally, we have shown that while the average IPR changes smoothly as $q$ changes at fixed $w$ or vice versa, the IPR *distribution* exhibits a very distinct (yet continuous) change as $q$ (or $w$) crosses a phase boundary, with IPR in the delocalized state having a peaked, mostly symmetric distribution but the IPR in the power-law localized and exponentially localized states having a highly skewed distribution with a peak near zero that becomes sharper as the particle becomes more localized. While we did not determine the phase boundaries independently using the IPR alone, we expect that the correspondence found here between delocalized/localized states and the IPR distribution will be useful in distinguishing delocalized states from localized ones in other scenarios, such as lattice configurations in which the appropriate extrapolation method for the thermodynamic limit is not necessarily clear.

# REFERENCES

# REFERENCES


[1] E. Abrahams, P.W. Anderson, D.C. Licciardello, and T.V. Ramakrishnan, Phys. Rev. Lett. **42**,673 (1979)

[2] P.W. Anderson, Phys. Rev. **109**, 1492 (1958)

[3] A. Eilmes, R. A. Römer, and M. Schreiber, Physica B **296**, 46 (2001)

[4] C. M. Soukoulis and E. N. Economou, Phys. Rev. Lett. **45**, 1590 (1980)

[5] P. A. Lee and D. S. Fisher, Phys. Rev. Lett. **47**, 882 (1981)

[6] A. MacKinnon and B. Kramer, Phys. Rev. Lett. **47**, 1546 (1981)

[7] N. Goldenfeld and R. Haydock, Phys. Rev. B **73**, 045118 (2006)

[8] H. Nakanishi and Md F. Islam, in *Quantum and Semi-classical Percolation and Breakdown in Disordered Solids*, edited by A. K. Sen, K. K. Bardhan, and B. K. Chakrabarti, Springer, pages 109–133, (2009)

[9] C. M. Soukoulis, E. N. Economou, and G. S. Grest, Phys. Rev. B **36**, 8649 (1987)

[10] Th. Koslowski and W. von Niessen, Phys. Rev. B **42**, 10342 (1990)

[11] I. Chang, Z. Lev, A.B. Harris, J. Adler, and A. Aharony, Phys. Rev. Lett. **74**, 2094 (1995)

[12] C. M. Soukoulis and G. S. Grest, Phys. Rev. B **44**, 4685 (1991)

[13] A. Mookerjee, I. Dasgupta, and T. Saha, Int. J. Mod. Phy. B **9**, (23), 2989 (1995)

[14] G. Hałdaś, A. Kolek, and A. W. Stadler, Phys. Status Solidi B **230**, 249 (2002)

[15] T. Odagaki and K. C. Chang, Phys. Rev. B **30**, 1612 (1984)

[16] V. Srivastava and M. Chaturvedi, Phys. Rev. B **30**, 2238 (1984)

[17] D. Daboul, I. Chang, and A. Aharony, Eur. Phys. J. B **16**, 303 (2000)

[18] H. N. Nazareno, P. E. de Brito, and E.S. Rodrigues, Phys. Rev. B **66**, 012205 (2002)

[19] G. Schubert and H. Fehske, Phys. Rev. B **77**, 245130 (2008)

[20] E. Cuansing and H. Nakanishi, Physica A **387**, 806 (2008)

[21] M.F. Islam and H. Nakanishi, Phys. Rev. E **77**, 061109 (2008)

[22] L. Gong and P. Tong Phys. Rev. B **80**, 174205 (2009)

[23] S. V. Kravchenko et al, Phys. Rev. B **50**, 8039 (1994)

[24] S. V. Kravchenko et al, Phys. Rev. B **51**, 7038 (1995)

[25] S. V. Kravchenko et al, Phys. Rev. B **59**, R12740 (1999)

[26] E. Abrahams, S. V. Kravchenko, and M. Sarachik, Rev. Mod. Phys. **73**, 251 (2001)

[27] L. Zhang et al, Science, **298**, 805 (2002)

[28] T. Becker et al, Phys. Rev. Lett. **89**, 237203 (2002)

[29] M. V. Feigel'man, A. S. Ioselevich, and M. A. Skvortsov, Phys. Rev. Lett. **93**, 136403 (2004)

[30] V. Cheianov et al, Phys. Rev. Lett. **99**, 176801 (2007)

[31] T. A. L. Ziman. Phys. Rev. B **26**, 7066 (1982)

[32] S. Johri and R. N. Bhatt, Phys. Rev. Lett. **109**, 076402 (2012)

[33] S. Johri and R. N. Bhatt, Phys. Rev. B **86**, 125140 (2012)

[34] Y. Wang, H. Hu, and S. Chen, Eur. Phys. J B **89**, 77 (2016)

[35] B. S. Dillon and H. Nakanishi, Eur. Phys. J B **87**, 286 (2014)

[36] J. W. Kantelhardt and A. Bunde, Ann. Phys. **7**, 400 (1998)

[37] G. Schubert and H. Fehske, In *Quantum and Semi-classical Percolation and Breakdown in Disordered Solids*, edited by A. K. Sen, K. K. Bardhan, and B. K. Chakrabarti, Springer, pages 163–189 (2009)

[38] E. P. Bernard and W. Krauth, Phys. Rev. Lett. **107**, 155704 (2011)

[39] J. M. Kosterlitz and D. J. Thouless, J. Phys. C **6**, 1181 (1973)

[40] C. M. Soukoulis, I. Webman, G. S. Grest, and E. N. Economou, Phys. Rev. B **26**, 1838 (1982)

[41] E. Cuansing and H. Nakanishi, Phys. Rev. E **70**, 066142 (2004)

[42] S. Kirkpatrick and T. P. Eggarter, Phys. Rev. B **6**, 3598 (1972)

[43] H.G. Schuster, Z. Phys. B **31**, 99 (1978)

[44] D. R. Nelson and B. I. Halperin, Phys. Rev. B **19**, 2457 (1979)

# APPENDICES

# A. ISOTROPIC LATTICE CODE (Cluster2DconstEpar.m)

Cluster2DconstEpar.m (below) is a Matlab function script used to calculate the transmission and reflection coefficients on a diluted lattice in the quantum percolation model, using the exact expression for the Schrödinger equation given in Eqn. 1.11.

**Inputs:**

**L**= lattice side length (number of sites = $L \times L$)

**E** = particle energy (same as in Eqn. 1.11)

**qmin** = minimum dilution for range modeled (in decimal form, not percentage)

**qmax** = maximum dilution for range modeled (in decimal form)

**qstep** = increment size between successive dilutions (i.e. $qnext = qprev + qstep$)

**ntot** = number of disorder realizations

**app** = identifying string suffix appended to data file (e.g. to distinguish different batches with same parameters)

**Output file:** L#_E#_q#ato#bparXYZsuffix.mat

(E.g. 'L10_E1.1_q10to20parRun1.mat')

**Output file contents:**

**qval** = vector of dilution values for which values were computed

**ref** = vector of average reflection coefficients $R$ for each dilution in $qval$

**tra** = vector of average transmission coefficients $T$ for each dilution in $qval$

**stdt** = vector of standard deviation of $T$ for each dilution in $qval$

**E** = particle energy used, same as input

**L** = lattice side length used, same as input

**tran** = matrix of individual transmission coefficients calculated for every disorder realization, used to compute $tra$. (row,col) = (disorder realization, dilution), that is,

each column contains all disorder realizations for a specific dilution.

Cluster2DconstEpar.m is called with different parameters in simulation scripts such as the following:

## Simulation script:

```
L=[443,368,312,261,215,181,151,126,105,88,74,62,52,44,37,31,...
      26,22,19,16,14,12,10];

matlabpool open local 7
%the above opens a pool of parallel workers in, needed for parfor
for i=1:1:length(L)
    rand('seed',10);
    L(i)
    Cluster2DconstEpar(L(i),1.1,0.02,0.12,0.02,500,'S11');
    Cluster2DconstEpar(L(i),1.1,0.15,0.36,0.03,1000,'S11');
end
matlabpool close
```

## Cluster2DconstEpar.m

```
function Cluster2DconstEpar(L,E,qmin,qmax,qstep,ntot,app)

warning off MATLAB:singularMatrix; %for small energies E, the matrix
% is close to singular; this line suppresses a warning to that effect

% construct the ordered Hamiltonian
```

```
% all non-zero elements are on main diagonal and 4 off-diagonals
% for maximum efficiency in diluting the lattice, the diagonals are
% initialized separately, then combined prior to final calculation,
% rather than initializing the entire hamiltonian at the outset

D=ones(L^2+2,1); % main diagonal
D=D.*-E;
q=acos(E/2);
i=sqrt(-1);
D(1,1)=D(1,1)+ exp(i*q);
D(L^2+2,1)=D(1,1);
b=sparse(L^2+2,1);
b(1)=2*i*sin(q);

Al=ones(L^2+2,1);% lower first diagonal
Al(L+1:L:L^2,1)=0;
Bl=ones(L^2+2,1); % Lth lower diagonal
Bl(1,1)=0;
Bl(L^2+2-L,1)=0;

Au=zeros(L^2+2,1); % upper first diagonal
for i=1:(L^2+1)
    Au(i+1,1)=Al(i,1);
end
Bu=zeros(L^2+2,1);% upper Lth diagonal
for i=1:(L^2+2-L)
    Bu(i+L)=Bl(i);
end
% sparse matrix for the undiluted lattice; used for code checks
```

```
% H=spdiags([Bl Al D Au Bu], [-L -1 0 1 L], L^2+2, L^2+2);

% initialize other variables
j=0;
numsteps=floor((qmax-qmin)/qstep)+1;
refl=zeros(ntot,numsteps);
tran=zeros(ntot,numsteps);
ref=zeros(1,numsteps);
tra=zeros(1,numsteps);
stdt=zeros(1,numsteps);

for qc=qmin:qstep:qmax
    j=j+1;
    tic;

    parfor n=1:ntot % automatically distributes iterations on workers
        warning off MATLAB:singularMatrix;
        if mod(n,100)==0
            fprintf('%u\n',n);
        end
        D1=D;% copy ordered Hamiltonian for diluting
        Al1=Al;
        Bl1=Bl;
       %k(n)=0; % optional code check to track disorder
        r=rand(L^2,1);
       % r is vector random numbers [0,1], one for each site, used to
       % randomly set disorder

        % the following loops set the disorder,
```

```
% while keeping the 9 sites nearest to input/output occupied.
for m=1:2
    for i=((m-1)*L+5):(m*L+1)
        if r(i-1)<qc
            %k(n)=k(n)+1; % increment disorder count check
            D1(i,1)=0;
            Al1(i-1,1)=0;
            Al1(i,1)=0;
            Bl1(i,1)=0;
            if((i-L)>0)
                Bl1(i-L,1)=0;
            end
        end
    end

    for i=((L-m)*L+2):((L-m+1)*L-2)
        if r(i-1)<qc
            %k(n)=k(n)+1;
            D1(i,1)=0;
            Al1(i-1,1)=0;
            Al1(i,1)=0;
            Bl1(i,1)=0;
            if((i-L)>0)
                Bl1(i-L,1)=0;
            end
        end
    end
end
```

```
for i=2*L+5:(L-2)*L-2
    if r(i-1)<qc
        %k(n)=k(n)+1;
        D1(i,1)=0;
        Al1(i-1,1)=0;
        Al1(i,1)=0;
        Bl1(i,1)=0;
        if((i-L)>0)
            Bl1(i-L,1)=0;
        end
    end
end

Au1=zeros(L^2+2,1);
for i=1:(L^2+1)
    Au1(i+1,1)=Al1(i,1);
end
Bu1=zeros(L^2+2,1);
for i=1:(L^2+2-L)
    Bu1(i+L)=Bl1(i);
end
% construct diluted lattice hamiltonian
H1=spdiags([Bl1 Al1 D1 Au1 Bu1], [-L -1 0 1 L], L^2+2, L^2+2);
% disorder set.

%d(n)=k(n)/(L^2);
% prev. line checks actual disorder percentage
x=H1\b; %calculate wavefunction
re=x(1)-1;
```

```
        t=x(length(x));
        if t~=t %NaN trap
            t=0;
        end
        if re~=re
            re=0;
        end
        refl(n,j)=re*conj(re);
        tran(n,j)=t*conj(t);
    end

    avgt=toc/ntot; %runtime calculation
    %dis(j)=sum(d)/ntot;       % optional disorder check
    %stdd(j)=std(d);
    ref(j)=sum(refl(1:ntot,j))/ntot; % average reflection coefficient
    tra(j)=sum(tran(1:ntot,j))/ntot; %average transmission coefficient
    stdt(j)=std(tran(1:ntot,j))/sqrt(ntot);

    fprintf('q=%d Runtime: %d seconds.\nPer disorder iteration: ...
                %d \n', qc, avgt*ntot, avgt);
end

qval=qmin:qstep:qmax;
fname=sprintf('L%d_E%0.2f_q%dto%dpar%s.mat', ...
       L, E,qmin*100,qmax*100,app);
save(fname,'qval','ref','tra','stdt','E','L','tran');
```

# B. ANISOTROPIC LATTICE CODE (Cluster2DconstEparStrip.m)

Cluster2DconstEparStrip.m (below) is a straightforward generalization of the code Cluster2DconstEpar.m (Appendix A) to $M \times N$ lattices. The other significant change is in how the random number generator seeding is handled. Matlab by default randomly seeds each worker, but in the same way with each initialization of the program, regardless of whether the main worker is seeded by Matlab's default or by the user. This did not influence the randomness of the results from Appendix A code, since the different selection of parameters (particularly of the disorder range and increment) ensured the rand calls would be applied differently. However, for subsequent computations I wanted more explicit control over the workers' random number seeding.

**Inputs:**

**E, qmin, qmax, qstep, ntot, app**= Same as in Appendix A code.

**M** = Width of lattice

**N** = Length of lattice

**stream** = Random number generator stream, set externally prior to function call. Controls how the stream is passed to the parallel workers that perform the disorder realization computation to ensure seeding of the random number generator in the main program carries over to the parallel workers.

**Output file:** L#_E#_q#ato#bparStripXYZsuffix.mat

(E.g. 'L10_E1.1_q10to20parStripRun1.mat')

**Output file contents:**

**qval, ref, tra, stdt, E, tran** = Same as in Appendix A code.

**M** = Width of lattice, same as input.

**N** = Length of lattice, same as input.

**p4sums** = matrix of $|\psi_i|^4$ values calculated for every disorder realization, used to compute the IPR. (row,col) = (disorder realization, dilution), that is, each column contains all disorder realizations for a specific dilution.

**S** = matrix of cluster size values (number of occupied non-zero-wavefunciton sites) on each disorder realization. (row,col) same as $p4sums$.

**Savg** = disorder average of $S$.

Cluster2DconstEparStrip.m is called in simulation scripts such as the following:

## Simulation script:

---

```
E=0.05
qmin=0.15
qmax=0.50
qstep=0.05
iter=1000
Nfactor=[200,100,90,80,70,60,55,50,45,40,38,36,34,32,30,28,26, ...
                24,22,20,19,18,17,16,15,14,13,12,11,10]

% Seed determined by running "rng('shuffle','combRecursive')" on
% Matlab command line to generate a seed based on current time,
% ensuring the seed used is appropriately random. I use this seed
% for all streams on a given round, so I don't seed the generator more
% than necessary; the difference in parameters is sufficient for a
% given round.

stream=RandStream('mrg32k3a','Seed',724207029)
```

```
RandStream.setGlobalStream(stream)

for i=1:length(Nfactor)
    sprintf('(M,Nf)=(8,%d)\n',Nfactor(i))
    job3=batch(@Cluster2DconstEparStrip,0,{8,Nfactor(i)*8,E,qmin, ...
                qmax,qstep,iter,stream,'Round1sup'},'matlabpool',11);
    wait(job3);  diary(job3); delete(job3);

    sprintf('(M,Nf)=(16,%d)\n',Nfactor(i))
    job3=batch(@Cluster2DconstEparStrip,0,{16,Nfactor(i)*16,E,qmin,...
                 qmax,qstep,iter,stream,'Round1sup'},'matlabpool',11);
    wait(job3);  diary(job3); delete(job3);
end
```

## Cluster2DconstEparStrip.m

---

```
function Cluster2DconstEparStrip(M,N,E,qmin,qmax,qstep,ntot,stream,app)

warning off MATLAB:singularMatrix;
%construct the ordered Hamiltonian
D=ones(M*N+2,1);
D=D.*-E;
q=acos(E/2);
i=sqrt(-1);
D(1,1)=D(1,1)+ exp(i*q);
D(M*N+2,1)=D(1,1);
b=sparse(M*N+2,1);
b(1)=2*i*sin(q);
```

```
Al=ones(M*N+2,1);
Al(N+1:N:M*N,1)=0;
Bl=ones(M*N+2,1);
Bl(1,1)=0;
Bl(N*M+2-N,1)=0;

Au=zeros(M*N+2,1);
for i=1:(M*N+1)
    Au(i+1,1)=Al(i,1);
end
Bu=zeros(M*N+2,1);
for i=1:(M*N+2-N)
    Bu(i+N)=Bl(i);
end

% ordered sparse matrix
%H2=spdiags([Bl Al D Au Bu], [-N -1 0 1 N], M*N+2, M*N+2)

%initialize other variables
j=0;
numsteps=floor((qmax-qmin)/qstep)+1;
refl=zeros(ntot,numsteps);
tran=zeros(ntot,numsteps);
p4sums=zeros(ntot,numsteps);
S=zeros(ntot,numsteps);
ref=zeros(1,numsteps);
tra=zeros(1,numsteps);
stdt=zeros(1,numsteps);
```

```
Savg=zeros(1,numsteps);

for qc=qmin:qstep:qmax
    j=j+1;
    tic;

    parfor n=1:ntot
        warning off MATLAB:singularMatrix;
        if mod(n,100)==0
            fprintf('%u\n',n);
        end
        D1=D;
        Al1=Al;
        Bl1=Bl;
        % the following two lines pass the random number generator
        % stream such that each iteration/realization starts at a
        % different location within the stream, thus ensuring that
        % the RAND seeding done in the simulation script is passed
        % on to Matlab's parallel workers.
        set(stream,'Substream',n);
        r=rand(stream,M*N,1);

        % the following loops set the disorder,
        % while keeping the 9 sites nearest to input/output occupied.
        for l=1:2
            for i=((l-1)*N+5):(l*N+1)
                if r(i-1)<qc
                    Al1(i-1,1)=0;
                    Al1(i,1)=0;
```

```
            Bl1(i,1)=0;
            if((i-N)>0)
                Bl1(i-N,1)=0;
            end
        end
    end

    for i=((M-l)*N+2):((M-l+1)*N-2)
        if r(i-1)<qc
            Al1(i-1,1)=0;
            Al1(i,1)=0;
            Bl1(i,1)=0;
            if((i-N)>0)
                Bl1(i-N,1)=0;
            end
        end
    end
end

for i=2*N+5:(M-2)*N-2
    if r(i-1)<qc
        Al1(i-1,1)=0;
        Al1(i,1)=0;
        Bl1(i,1)=0;
        if((i-N)>0)
            Bl1(i-N,1)=0;
        end
    end
end
```

```
Au1=zeros(M*N+2,1);
for i=1:(M*N+1)
    Au1(i+1,1)=Al1(i,1);
end
Bu1=zeros(M*N+2,1);
for i=1:(M*N+2-N)
    Bu1(i+N)=Bl1(i);
end
% construct diluted lattice hamiltonian
H1=spdiags([Bl1 Al1 D1 Au1 Bu1], [-N -1 0 1 N], M*N+2, M*N+2);
% disorder set.

x=H1\b;
psi=x(2:(length(x)-1));
psi2=psi.*conj(psi);
Nfactor=sqrt(1/nansum(psi2));
psinorm=Nfactor*psi;
psi4sum=nansum((psinorm.*conj(psinorm)).^2);
Sn=sum(~isnan(psinorm))-length(find(psinorm==0));
% Sn does not check for connectivity, just counts
% sites that are available and have nonzero wavefunction
% Note that when checking over length of vector, 0s are not
% excluded in the counting to determine iszero or isnan, thus
% must do explicit check for these when calculating Sn.

re=x(1)-1;
t=x(length(x));
if t~=t %NaN trap
```

```
            t=0;
        end
        if re~=re
            re=0;
        end
        refl(n,j)=re*conj(re);
        tran(n,j)=t*conj(t);
        p4sums(n,j)=psi4sum;
        S(n,j)=Sn;
    end

    avgt=toc/ntot;
    ref(j)=sum(refl(1:ntot,j))/ntot; %average reflection coefficient
    tra(j)=sum(tran(1:ntot,j))/ntot; %average transmission coefficient
    stdt(j)=std(tran(1:ntot,j))/sqrt(ntot);
    Savg(j)=sum(1./p4sums(1:ntot,j)./S(1:ntot,j))/ntot;

    fprintf('q=%d Runtime: %d seconds.\nPer disorder iteration: ...
               %d \n', qc, avgt*ntot, avgt);
end

qval=qmin:qstep:qmax;
fname=sprintf('M%dN%d_E%0.2f_q%dto%dparStrip%s.mat', ...
                       M,N, E,qmin*100,qmax*100,app);
save(fname,'qval','ref','tra','stdt','E','M','N', ...
          'tran','p4sums','S','Savg');
```

# C. SYMBOLIC MATH CALCULATIONS (symtest.m)

A code block that solves the quantum percolation problem algebraically rather than numerically for one specific disorder realization only, using Matlab's symbolic math toolbox and variable-precision architecture (vpa). The code was copy-pasted into Matlab command line after defining the vpa precision using the "digits" function. Viewing saved results after calculations: to see full-precision output of final output variables (x/t/re/tran/refl) set digits(#) where # is precision that was set prior to symbolic calculation, then do vpa(varname) where varname = x, t, re.... You will find that vpa(refl0) experiences round-off to 1 for sufficiently small transmission while vpa(refl) does not, and vpa(tran) and vpa(tran0) match for a sufficient number of digits in double precision if not out to all 16 digits in double precision.

## symtest.m

---

```
% The first section sets up the problem using the original method
% for *one* disorder realization, to compare with the algebraic
% solution in the next section. For this portion, define E, qc, M,
% and N in the commandline first.
D=ones(M*N+2,1);
D=D.*-E;
q=acos(E/2);
i=sqrt(-1);
D(1,1)=D(1,1)+ exp(i*q);
D(M*N+2,1)=D(1,1);
b=sparse(M*N+2,1);
```

```
b(1)=2*i*sin(q);

Al=ones(M*N+2,1);
Al(N+1:N:M*N,1)=0;
Bl=ones(M*N+2,1);
Bl(1,1)=0;
Bl(N*M+2-N,1)=0;

Au=zeros(M*N+2,1);
for i=1:(M*N+1)
    Au(i+1,1)=Al(i,1);
end
Bu=zeros(M*N+2,1);
for i=1:(M*N+2-N)
    Bu(i+N)=Bl(i);
end
% ordered sparse matrix
%H2=spdiags([Bl Al D Au Bu], [-N -1 0 1 N], M*N+2, M*N+2)

D1=D;
Al1=Al;
Bl1=Bl;
%set disorder
r=rand(M*N,1);

for l=1:2
    for i=((l-1)*N+5):(l*N+1)
        if r(i-1)<qc
            Al1(i-1,1)=0;
```

```
            Al1(i,1)=0;
            Bl1(i,1)=0;
            if((i-N)>0)
                Bl1(i-N,1)=0;
            end
        end
    end

    for i=((M-l)*N+2):((M-l+1)*N-2)
         if r(i-1)<qc
            Al1(i-1,1)=0;
            Al1(i,1)=0;
            Bl1(i,1)=0;
            if((i-N)>0)
                Bl1(i-N,1)=0;
            end
        end
   end
end

for i=2*N+5:(M-2)*N-2
    if r(i-1)<qc
        Al1(i-1,1)=0;
        Al1(i,1)=0;
        Bl1(i,1)=0;
        if((i-N)>0)
            Bl1(i-N,1)=0;
        end
    end
```

```
end

Au1=zeros(M*N+2,1);
for i=1:(M*N+1)
    Au1(i+1,1)=Al1(i,1);
end
Bu1=zeros(M*N+2,1);
for i=1:(M*N+2-N)
    Bu1(i+N)=Bl1(i);
end
% diluted lattice hamiltonian
H1=spdiags([Bl1 Al1 D1 Au1 Bu1], [-N -1 0 1 N], M*N+2, M*N+2);

%computations doen with the "original" method
x0=H1\b;
re0=x0(1)-1;
t0=x0(length(x0));
refl0=re0*conj(re0);
tran0=t0*conj(t0);

%computations with higher-precision symbolic math
% toolbox from numeric matrices
x=sym(H1)\sym(b);
re=x(1)-1;
t=x(length(x));
refl=re*conj(re);
tran=t*conj(t);

%same as x/re/t etc but with floating point
```

```
% numbers instead of doubles
x2=sym(H1,'f')\sym(b,'f');
re2=x2(1)-1;
t2=x2(length(x2));
refl2=re2*conj(re2);
tran2=t2*conj(t2);

%%% Second method done using the symbolic math toolbox to solve the
% matrix equation algebraically. Must provide M, N, and qc values,
% with E able to be inserted later.

syms D E q i b Al Bl  %symbolic math variables
D=ones(M*N+2,1);
D=D.*-E;
q=acos(E/2);
i=sym(sqrt(-1))
D(1,1)=D(1,1)+ exp(i*q);
D(M*N+2,1)=D(1,1);
b=sym(sparse(M*N+2,1));
b(1)=2*i*sin(q);

Al=sym(ones(M*N+2,1));
Al(N+1:N:M*N,1)=0;
Bl=sym(ones(M*N+2,1));
Bl(1,1)=0;
Bl(N*M+2-N,1)=0;

Au=zeros(M*N+2,1);
for i=1:(M*N+1)
```

```
    Au(i+1,1)=Al(i,1);
end
Bu=zeros(M*N+2,1);
for i=1:(M*N+2-N)
    Bu(i+N)=Bl(i);
end

D1=D;
Al1=Al;
Bl1=Bl;

% Use same r=rand(M*N,1) as first section in
% order to use same disorder realization
for l=1:2
    for i=((l-1)*N+5):(l*N+1)
        if r(i-1)<qc
            Al1(i-1,1)=0;
            Al1(i,1)=0;
            Bl1(i,1)=0;
            if((i-N)>0)
                Bl1(i-N,1)=0;
            end
        end
    end

    for i=((M-l)*N+2):((M-l+1)*N-2)
        if r(i-1)<qc
            Al1(i-1,1)=0;
            Al1(i,1)=0;
```

```
            Bl1(i,1)=0;
            if((i-N)>0)
                Bl1(i-N,1)=0;
            end
        end
    end
end

for i=2*N+5:(M-2)*N-2
    if r(i-1)<qc
        Al1(i-1,1)=0;
        Al1(i,1)=0;
        Bl1(i,1)=0;
        if((i-N)>0)
            Bl1(i-N,1)=0;
        end
    end
end

Au1=zeros(M*N+2,1);
for i=1:(M*N+1)
    Au1(i+1,1)=Al1(i,1);
end
Bu1=zeros(M*N+2,1);
for i=1:(M*N+2-N)
    Bu1(i+N)=Bl1(i);
end

% diluted lattice hamiltonian in symbolic math format
```

```
H1=diag(Bl(1:(M*N+2-N)),-N)+diag(Al(1:M*N+1),-1)+ ...
               diag(D,0)+diag(Al(1:M*N+1),1)+diag(Bl(1:(M*N+2-N)),N);

%computed with all matrices in symbolic (algebraic) format
% to begin with, computation at very end.
x=sym(H1)\sym(b);
re=x(1)-1;
t=x(length(x));
refl=re*conj(re);
tran=t*conj(t);
```

# D. NON-0 HOPPING INTEGRAL CODE (Cluster2DconstEparStripWeak.m)

Cluster2DconstEparStripWeak.m (below) is a straightforward generalization of the code Cluster2DconstEpar.m (Appendix A) to $M \times N$ lattices with non-zero diluted site hopping integrals (aka "weak bonds"). It is almost the same as Cluster2DconstEparStrip.m (Appendix B), the main difference being that the diluted-site hopping energy is set to a variable value, which necessitates a check to avoid changing boundary conditions when diluting the lattice (unnecessary on the original model code). The random number generator stream is passed in the same manner as Cluster2DconstEparStrip.m in Appendix B. In this work, I used isotropic lattices for which $M = N$.

**Inputs:**

**M, N, E, qmin, qmax, qstep, ntot, stream, app**= Same as in Appendix B code.

**w** = Value of hopping integral $V_{ij}$ for diluted sites (range: [0,1])

**Output file:** L#_E#_q#ato#bparStripWeakXYZsuffix.mat

(E.g. 'L10_E1.1_q10to20parStripWeakRun1.mat')

**Output file contents:**

**qval, ref, tra, stdt, E, M, N, tran, p4sums, S, Savg** = Same as in Appendix B code.

**w** = same as input.

Cluster2DconstEparStripWeak.m is called with different parameters in simulation scripts such as the following:

## Simulation script:

```
L=[368,261,181,151,88,74,62,52,44,37,26,22,19,16,14,12];
w=[1,0.99,0.98,0.97,0.96,0.95];
suff=cellstr(['1    ';'0_99 ';'0_98 ';'0_97 ';'0_96 ';'0_95 ']);
stream=RandStream('mrg32k3a')
RandStream.setGlobalStream(stream)

for i=1:length(L)
  for j=1:length(w)
     job1=batch(@Cluster2DconstEparStripWeak,0,{L(i),L(i),0.1,w(j)...
         0.02,0.12,0.02,500,stream,char(suff(j))},'matlabpool',11);
     wait(job1);  diary(job1); delete(job1);
     job1=batch(@Cluster2DconstEparStripWeak,0,{L(i),L(i),0.1,w(j),...
          0.15,0.35,0.05,1000,stream,char(suff(j))},'matlabpool',11);
     wait(job1);  diary(job1); delete(job1);
  end
end
```

## Cluster2DconsteEparStripWeak.m

```
function Cluster2DconstEparStripWeak(M,N,E,w,qmin,qmax,qstep,ntot,stream,app)
warning off MATLAB:singularMatrix;

%construct the ordered Hamiltonian
```

```
D=ones(M*N+2,1);
D=D.*-E;
q=acos(E/2);
i=sqrt(-1);
D(1,1)=D(1,1)+ exp(i*q);
D(M*N+2,1)=D(1,1);
b=sparse(M*N+2,1);
b(1)=2*i*sin(q);

Al=ones(M*N+2,1);
Al(N+1:N:M*N,1)=0;
Bl=ones(M*N+2,1);
Bl(1,1)=0;
Bl(N*M+2-N,1)=0;

Au=zeros(M*N+2,1);
for i=1:(M*N+1)
    Au(i+1,1)=Al(i,1);
end
Bu=zeros(M*N+2,1);
for i=1:(M*N+2-N)
    Bu(i+N)=Bl(i);
end
% ordered sparse matrix
%H2=spdiags([Bl Al D Au Bu], [-N -1 0 1 N], M*N+2, M*N+2)

%initialize other variables
j=0;
numsteps=floor((qmax-qmin)/qstep)+1;
```

```
refl=zeros(ntot,numsteps);
tran=zeros(ntot,numsteps);
p4sums=zeros(ntot,numsteps);
S=zeros(ntot,numsteps);
ref=zeros(1,numsteps);
tra=zeros(1,numsteps);
stdt=zeros(1,numsteps);
Savg=zeros(1,numsteps);

for qc=qmin:qstep:qmax
    j=j+1;
    tic;

    parfor n=1:ntot
        warning off MATLAB:singularMatrix;
        if mod(n,100)==0
            fprintf('%u\n',n);
        end
        D1=D;
        Al1=Al;
        Bl1=Bl;
        % the following two lines pass the random number generator
        % stream such that each iteration/realization starts at a
        % different location within the stream, thus ensuring that
        % the RAND seeding done in the simulation script is passed
        % on to Matlab's parallel workers.
        set(stream,'Substream',n);
        r=rand(stream,M*N,1);
```

```
% the following loops set the disorder,
% while keeping the 9 sites nearest to input/output occupied.
for l=1:2
    for i=((l-1)*N+5):(l*N+1)
        if r(i-1)<qc
           % if-statement maintains boundary conditions,
           % not needed when w=0.
            if(Al1(i-1,1)==1)
                 Al1(i-1,1)=w;
            end
            if(Al1(i,1)==1)
                Al1(i,1)=w;
            end
            if(Bl1(i,1)==1)
                Bl1(i,1)=w;
            end
            if((i-N)>0)
                if(Bl1(i-N,1)==1)
                    Bl1(i-N,1)=w;
                end
            end
        end
    end

    for i=((M-l)*N+2):((M-l+1)*N-2)
        if r(i-1)<qc
            if(Al1(i-1,1)==1)
                Al1(i-1,1)=w;
            end
```

```
            if(Al1(i,1)==1)
                Al1(i,1)=w;
            end
            if(Bl1(i,1)==1)
                Bl1(i,1)=w;
            end
            if((i-N)>0)
                if(Bl1(i-N,1)==1)
                    Bl1(i-N,1)=w;
                end
            end
        end
    end
end

for i=2*N+5:(M-2)*N-2
    if r(i-1)<qc
        if(Al1(i-1,1)==1)
            Al1(i-1,1)=w;
        end
        if(Al1(i,1)==1)
            Al1(i,1)=w;
        end
        if(Bl1(i,1)==1)
            Bl1(i,1)=w;
        end
        if((i-N)>0)
            if(Bl1(i-N,1)==1)
                Bl1(i-N,1)=w;
```

```
            end
        end
    end
end

Au1=zeros(M*N+2,1);
for i=1:(M*N+1)
    Au1(i+1,1)=Al1(i,1);
end
Bu1=zeros(M*N+2,1);
for i=1:(M*N+2-N)
    Bu1(i+N)=Bl1(i);
end
% construct diluted lattice hamiltonian
H1=spdiags([Bl1 Al1 D1 Au1 Bu1], [-N -1 0 1 N], M*N+2, M*N+2);

x=H1\b;
psi=x(2:(length(x)-1));
psi2=psi.*conj(psi);
Nfactor=sqrt(1/nansum(psi2));
psinorm=Nfactor*psi;
psi4sum=nansum((psinorm.*conj(psinorm)).^2);
Sn=sum(~isnan(psinorm))-length(find(psinorm==0));
% Sn does not check for connectivity, just counts
% sites that are available and have nonzero wavefunction
% Note that when checking over length of vector, 0s are not
% excluded in the counting to determine iszero or isnan, thus
% must do explicit check for these when calculating Sn.
```

```
        re=x(1)-1;
        t=x(length(x));
        if t~=t %NaN trap
            t=0;
        end
        if re~=re
            re=0;
        end
        refl(n,j)=re*conj(re);
        tran(n,j)=t*conj(t);
        p4sums(n,j)=psi4sum;
        S(n,j)=Sn;
    end

    avgt=toc/ntot;
    ref(j)=sum(refl(1:ntot,j))/ntot; %average reflection coefficient
    tra(j)=sum(tran(1:ntot,j))/ntot; %average transmission coefficient
    stdt(j)=std(tran(1:ntot,j))/sqrt(ntot);
    Savg(j)=sum(1./p4sums(1:ntot,j)./S(1:ntot,j))/ntot;

    fprintf('q=%d Runtime: %d seconds.\nPer disorder iteration: ...
             %d \n', qc, avgt*ntot, avgt);
end

qval=qmin:qstep:qmax;
fname=sprintf('M%dN%d_E%0.2f_q%dto%dparStripWeak%s.mat', ...
            M,N,E,round(qmin*100),round(qmax*100),app);
save(fname,'qval','ref','tra','stdt','E','w','M','N', ...
         'tran','p4sums','S','Savg');
```

VITA

# VITA

Brianna S. Dillon Thomas graduated Summa Cum Laude from Grove City College in 2010 with a B.S. in Applied Physics and a Minor in Mathematics. While a student at Grove City College, she participated in two summer Research Experiences for Undergraduates at other universities: experimental fiber optics on tellurite fibers with Jean Toulouse at Lehigh University in 2008, and computational condensed matter physics research on the Blume-Capel model with Richard Scalettar at U.C. Davis in 2009, the latter of which resulted in a paper in Physical Review B in 2010. She also presented her fiber optics research at the 2008 Society of Physics Students Quadrennial Congress poster session, and gave a seminar on her Blume-Capel research at Grove City College's student research seminar series. Outside of classes, she was highly active in Grove City College's Society of Physics Students Chapter, serving as secretary and treasurer, and as vice-president of the honorary Sigma Pi Sigma, during which time she co-organized a regional Zone meeting with nearly 100 undergraduate attendees.

Brianna began graduate studies at Purdue University in August 2010, and began working with Hisao Nakanishi in the Summer of 2012. Her first paper on quantum percolation, "Localization phase diagram of two-dimensional quantum percolation", was published in the European Physical Journal B in 2014. As of the completion of her Ph.D., she has a second paper under review and a third manuscript under preparation. In addition to her Ph.D. studies, she has also completed a concentration in Computational Science through Purdue University's Computational Interdisciplinary Graduate Program, and has pursued opportunities to improve and inform her teaching skills through the Department of Physics and Astronomy's Physics Education Research seminars and journal clubs. During her time at Purdue, she has given contributed talks at the 2014, 2015, and 2016 APS March meetings and the

109th Statistical Mechanics Conference at Rutgers University. She has also received multiple internal fellowships and awards: the Purdue University Ross Fellowship, the Physics Department Fellowship, the Lijuan Wang Award for outstanding female graduate student in physics, and the first Charlotte Ida Litman Tubis Award for clear and concise communication of physics to a lay audience.

Upon graduation, Brianna will be a Visiting Assistant Professor of Physics at St. Olaf College in Northfield, MN.